HIGH-PRECISION MEASUREMENTS OF THE SUPERALLOWED β^+ DECAYS OF ^{38}Ca AND ^{46}V

A Dissertation

by

HYO-IN PARK

Submitted to the Office of Graduate Studies of
Texas A&M University
in partial fulfillment of the requirements for the degree of

DOCTOR OF PHILOSOPHY

August 2011

Major Subject: Physics

HIGH-PRECISION MEASUREMENTS OF THE SUPERALLOWED β^+ DECAYS OF ^{38}Ca AND ^{46}V

A Dissertation

by

HYO-IN PARK

Submitted to the Office of Graduate Studies of
Texas A&M University
in partial fulfillment of the requirements for the degree of

DOCTOR OF PHILOSOPHY

Approved by:

Chair of Committee,	John C. Hardy
Committee Members,	Carl A. Gagliardi
	Robert E. Tribble
	Sherry J. Yennello
Head of Department,	Edward S. Fry

August 2011

Major Subject: Physics

ABSTRACT

High-Precision Measurements of the Superallowed β^+ Decays of ^{38}Ca and ^{46}V.

(August 2011)

Hyo-In Park, B.S., Colorado State University;

M.S., University of Tennessee

Chair of Advisory Committee: John C. Hardy

As a part of our program to test the unitarity of the Cabibbo-Kobayashi-Maskawa matrix, the decay of the superallowed $0^+ \rightarrow 0^+$ beta emitters ^{38}Ca and ^{46}V has been studied in this dissertation.

For ^{38}Ca, the half-life, 443.88(36) ms, and superallowed branching ratio, 0.7738(41), have been measured. In our half-life experiment, pure sources of ^{38}Ca were produced and the decay positrons detected in a high-efficiency 4π proportional gas counter. Since the β^+ decay of ^{38}Ca feeds ^{38}K^m, which is itself a superallowed β^+ emitter, the data were analyzed as a linked parent-daughter decay. Our result for the half-life of ^{38}Ca, with a precision of 0.08%, is a factor of five improvement on the best previous result. The branching-ratio of ^{38}Ca depended on β-delayed γ-ray intensities being measured with a high-purity germanium detector calibrated for absolute efficiency to 0.2% precision. This branching-ratio result represents our first step in bringing the ft value for the superallowed ^{38}Ca transition into the desired range of 0.1%. With our half-life and superallowed branching ratio results for ^{38}Ca, we obtain the $\mathcal{F}t$ to be 3072(17) s, in good agreement with the conserved vector current expectation.

The half-life of ^{46}V has been measured to be 422.66(6) ms, a factor of two more precise than the best previous measurement. Our present result determines the corresponding $\mathcal{F}t$ value to be 3074.5(26) s, which is consistent with the average $\overline{\mathcal{F}t}$ value

of 3072.08(79) s established from the 13 best-known superallowed transitions. This demonstrates that previously accepted half-lives of ^{46}V were correct in their contribution to a precision test of the conserved vector current hypothesis.

To my parents

ACKNOWLEDGMENTS

It is my pleasure to express my deep appreciation to all members of the Cyclotron Institute at Texas A&M University. I have been so fortunate to be a part of this wonderful group who made my experience a great reality every day and provided a nice environment in which to conduct my research.

I would like to express my sincere gratitude to my advisor, Distinguished Professor John C. Hardy, for his determination, guidance, and support. He showed me the real significance of not only working hard to become a competent physicist but also enjoying each step of the journey through life. I must admit that his integrity was a constant inspiration.

I like to extend my special thanks to Dr. Victor E. Iacob. Without his tremendous help, this work could not have been completed. His support and comments in the final stages of preparation of this work are deeply appreciated. I also thank Dr. Victor V. Golovko for being a good friend and for introducing me to the world of programming.

I would like to thank my committee members, Professor Carl A. Gagliardi, Distinguished Professor Robert E. Tribble and Professor Sherry J. Yennello, for their generous advice and insight on this dissertation. I am very grateful that they enlightened me about various topics in the field of weak interaction. I especially thank Professor Ian S. Towner for his careful review on the theory section of this dissertation and for many informative discussions to challenge me on the theoretical issues of this work.

Many thanks go to Dr. George Kim, Dr. Don May and Dr. Livius Trache for providing high-purity radioactive ion-beams. I also thank my collaborators who shared the long and difficult beam times with me. They are Dr. Adriana Banu, Dr.

Lixin Chen, Dr. Vladimir Horvat, Matthew McClesky, Dr. Ninel Nica, Dr. Brian Roeder and Ellen Simmons.

Equal thanks go to my friends, Matt Cervantes, Jim Drachenberg, Dr. Pibero Djawotho, and Dr. Hyunjeong Kim, for all of the intriguing discussions on physics, high technology, classical music, history and world. Especially, I would like to give my greatest thanks to my roommate, Jooah Kang. I will miss the wonderful times we shared different perspectives from our lives and the moments we simply laughed.

I am immensely grateful to my family who stood by me for my entire life. Thank you Mom and Dad for your love, devotion and respect. Thanks to Jung-Shik for your unconditional prayers and care. Finally, I give all my gratitude and praise to the Lord who gave me the light in a world of darkness through the resurrection of Jesus Christ.

TABLE OF CONTENTS

CHAPTER Page

LIST OF TABLES

LIST OF FIGURES

FIGURE Page

FIGURE Page

FIGURE Page

FIGURE Page

CHAPTER I

INTRODUCTION

At present, the most stringent test of the unitarity of the Cabibbo-Kobayashi-Maskawa (CKM) matrix depends on results from superallowed $0^+ \rightarrow 0^+$ nuclear β decay. Precise measurements of ft values for these superallowed transitions provide a direct determination of the weak vector coupling constant G_V within an uncertainty of $\pm 0.013\%$ and lead to the most precise value of V_{ud}, the up-down quark-mixing element of the CKM matrix, within $\pm 0.023\%$ [1]. Incorporating this result, the sum of squares of the top-row elements of the CKM matrix satisfies the unitarity condition at the level of $\pm 0.06\%$ [1]. This remarkable agreement with the standard model constrains the scope of any new physics possible beyond the standard model, and motivates the quest for still higher experimental precision to make the unitarity test even more definitive. The work presented here is part of our program at Texas A&M University to increase the number of precisely measured transitions. We focus on measuring the half-life and branching ratio for the superallowed β^+ emitter, ^{38}Ca (T_Z = -1) and the half-life of ^{46}V ($T_Z = 0$).

To extract V_{ud} from experimental data, accurate calculations of small nuclear-structure-dependent corrections are essential to account for unobserved radiative effects as well as isospin-symmetry breaking between the analog parent and daughter states of each superallowed transition. Currently uncertainties in these calculations are comparable to the present level of experimental precision. However, these theoretical uncertainties can, in principle, be reduced by improving the precision of the experimental ft values, and the efficacy of these correction terms can be tested based

---

The journal model is Physical Review C.

on the corrected $\mathcal{F}t$ values being required to satisfy the conserved vector current (CVC) hypothesis. The case of ^{38}Ca—a nucleus whose superallowed decay is not yet fully characterized—is particularly interesting in this regard, since its total nuclear-structure-dependent correction is calculated with the effective-interaction shell model combined with Saxon-Woods radial wave functions to be $\delta_C - \delta_{NS} = 0.94(7)\%$, one of the largest in the *sd* shell [2]. If, with such a large correction, the measured ft value for ^{38}Ca were also to yield a corrected $\mathcal{F}t$ value consistent with the average established from the 13 currently best-known cases, then it would become a further powerful experimental validation of the calculated corrections. Essential to this test and to placing ^{38}Ca on the same footing as the other well-known cases is a measurement of the ft value for its superallowed $0^+ \rightarrow 0^+$ beta transition with $\sim 0.1\%$ precision or better. We report our measured half-life and the first preliminary results from a branching-ratio measurement. Combined with the well-known Q_{EC} value [3, 4, 5], these two results will ultimately lead to a precise $\mathcal{F}t$ value for ^{38}Ca, and a valuable test of the calculated nuclear-structure-dependent correction term.

The decay of ^{46}V was the first of the nine best-known superallowed transitions to have its Q_{EC} value measured (in 2005) with an on-line Penning trap [6]. The result differed significantly from the previously accepted result – a longstanding reaction-based Q_{EC} value [7] – and shifted the ^{46}V ft value two standard deviations out of agreement with other well-known superallowed transitions. This apparent deviation from the CVC expectation raised several concerns, among them the possibility of systematic differences between reaction and Penning-trap measurements of Q values. As a result, another independent Penning-trap measurement was performed a year later, in which the Q_{EC} value for ^{46}V was determined again, along with the Q_{EC} values for two other superallowed beta emitters, ^{26}Al^m and ^{42}Sc [8]. The second measurement for ^{46}V confirmed the first Penning-trap result. At the same time though, the Q_{EC}-

value results for $^{26}\mathrm{Al}^{m}$ and $^{42}\mathrm{Sc}$ were consistent with previous reaction-based values, thus demonstrating that there were no widespread systematic effects afflicting all reaction-based measurements. Evidently, the problem with the $^{46}\mathrm{V}$ Q_{EC} value arose from some flaw specific to one particular set of reaction measurements [7]. This conclusion was further strengthened by a subsequent Q-value measurement [9] (in 2009), which used the same ($^{3}\mathrm{He}$, t) reaction and some of the same equipment as had been used in the earlier flawed measurement. It obtained a Q_{EC} value for $^{46}\mathrm{V}$ that was entirely consistent with the two Penning trap results.

In parallel with these experimental studies, the theory used in the analysis of the $^{46}\mathrm{V}$ results was carefully reexamined as well. In order to extract G_V from a measured ft value, radiative and isospin-symmetry-breaking corrections must both be applied to convert the measured ft value into a corrected $\mathcal{F}t$ value [10]. In the case of $^{46}\mathrm{V}$ and the other $f_{7/2}$-shell nuclei, the original isospin-symmetry-breaking corrections had been derived with a shell model based on a closed sd shell at $^{40}\mathrm{Ca}$. However the presence of low-lying $3/2^{+}$ and $1/2^{+}$ states in $^{45}\mathrm{Ti}$ and other nuclei in the region shows that core orbitals must play an important role. Accordingly, the isospin-symmetry-breaking corrections were improved [2] by the inclusion of core orbitals in the model space used in the calculation. The choice of which orbitals to include was guided by the measured spectroscopic factors for single-nucleon pickup reactions on the nuclei of interest. This improvement had the largest effect on the $^{46}\mathrm{V}$ transition, but also had smaller effects on other superallowed transitions, especially on those in the $f_{7/2}$ shell. These new corrections, which were incorporated into the most recent survey of world data [10], eliminated the $^{46}\mathrm{V}$ anomaly, restored the consistency with CVC and retained agreement with CKM matrix unitarity.

All these experimental and theoretical studies have proceeded under the tacit assumption that the previously accepted half-life of $^{46}\mathrm{V}$ was completely correct. Al-

though there was no reason to suspect that this half-life result was in error, there had not been any reason to suspect that there was anything wrong with the now-discredited Q_{EC} value either. We have addressed this potential weakness and report here on a new measurement of the ^{46}V half-life, which confirms the average of previous measurements but is a factor of two more precise than the best of them.

In this dissertation, we begin by describing the framework and formalism related to the properties of the weak interaction in nuclear β decay. Then, for our half-life and branching-ratio measurements, a detailed description of the experimental setup and procedures is provided with an emphasis on different detection arrangement. Our experimental analysis and results for ^{38}Ca and ^{46}V are followed by conclusions.

CHAPTER II

WEAK INTERACTION AND NUCLEAR β DECAY

Since the discovery of radioactivity by Becquerel in 1896, studies of nuclear β decay have significantly contributed to the development of weak interaction theory. Maximal parity violation, the two-component neutrino, and the vector-axial vector nature of the weak interaction were discovered in nuclear β decay [11]. In this chapter, the main aspects of the standard model relevant to nuclear β decay are briefly reviewed. The framework for the determination of precise ft values in superallowed Fermi β decay is provided and the impact it has on the unitarity test of the Cabibbo-Kobayashi-Maskawa (CKM) matrix is discussed.

A. Quarks and leptons in the weak interaction

Two classes of fermions, quarks and leptons, together with the gauge bosons are the fundamental constituents of our universe. Six quarks and leptons are characterized by mass into three generations. Each generation contains two quarks and two leptons. The mass of particles becomes heavier as the generation number increases from the first to the third. The names of these particles, together with their electric charges are presented in Table I. For every particle, there is an antiparticle with opposite charge and magnetic moment, but with the same mass and lifetime. Nucleons are composite particles made up of the lightest up and down quarks *i.e.*, the proton is *uud* and the neutron *udd*.

Such particles experience the weak interaction that governs nuclear β decay. In 1934, Fermi hypothesized [12] a vector-vector, local, four-fermion interaction between a hadronic current, $J_{\mu}^{(n\to p)} = \overline{\psi_p}\gamma_{\mu}\psi_n$, and a leptonic current, $J^{\mu}_{(\nu\to e)} = \overline{\psi_e}\gamma^{\mu}\psi_{\nu}$, in neutron β decay in exactly analogous manner to the way the electromagnetic

Table I. Quark and lepton flavors

Generation	Symbol	Name	Q/$\|e\|$	Symbol	Name	Q/$\|e\|$
First	u	up	$+2/3$	e	electron	-1
	d	down	$-1/3$	ν_e	e-neutrino	0
Second	c	charm	$+2/3$	μ	muon	-1
	s	strange	$-1/3$	ν_μ	μ-neutrino	0
Third	t	top	$+2/3$	τ	tau	-1
	b	bottom	$-1/3$	ν_τ	τ-neutrino	0

interaction is written

$$\mathcal{L}_\beta = G_V J_\mu^{(n\to p)} J^\mu_{(\nu\to e)} = G_V(\overline{\psi_p}\gamma_\mu\psi_n)(\overline{\psi_e}\gamma^\mu\psi_\nu), \tag{2.1}$$

where ψ_p, ψ_n, ψ_e, and ψ_ν are the wavefunctions of proton, neutron, electron, and neutrino, respectively. The so-called Fermi coupling constant, G_V, characterizes the strength of the weak interaction, similar to the electric charge, e, that characterizes the strength of the electromagnetic interaction.

In the modern theory of the standard model, the left-handed vector gauge bosons, $W^\pm$ and Z^0, mediate the charged-current and the neutral- current weak interactions as a consequence of electroweak unification. Their large masses, $m_W = 80.399(23)\ GeV/c^2$ and $m_Z = 91.1876(21)\ GeV/c^2$, result in the extremely short-range (of order $1/m_W \approx 0.001\ fm$) nature of the weak interaction. Thus the four fermion contact interaction in Fermi's model is valid to a very good approximation for all nuclear β decays.

B. Conserved vector current hypothesis

It was a striking result that the experimentally determined coupling constants from nuclear β decay and the purely leptonic μ decay were very similar to each other even though nuclear β decay involves composite particles and would be expected to have renormalization effects from the virtual emission and absorption of pions and baryons [13]. To explain this close agreement, Feynman and Gell-Mann proposed that the weak-interaction vector current, like the electromagnetic interaction, is a conserved current [14]. This postulate is known as the conserved vector current (CVC) hypothesis. Since the coupling strength, e, with the electromagnetic field, is the same for all particles coupled, by analogy the vector coupling constant, G_V, should be universal if the vector current of the weak interaction is conserved. The CVC can be tested in nuclear β via superallowed $0^+ \longrightarrow 0^+$ transitions. The determined vector coupling constants from many superallowed transitions should always be the same, independent of the nuclear medium in which the decay occurs. Further discussion about this experimental test of the CVC is given in Sec. II.D.2 and Sec. II.E.

C. The Cabibbo-Kobayashi-Maskawa quark-mixing matrix

The large difference of the measured strengths between strangeness-conserving and strangeness-changing leptonic processes cannot be explained by the universal Fermi interaction [15]. Although a modification of universality seemed to be necessary, Cabibbo proposed [16] the idea of unitary symmetry by modifying the hadronic weak current in terms of the so-called Cabibbo angle, θ_c, instead of introducing a new coupling constant for strange particle decays. The insight of Cabibbo mixing was generalized later by Kobayashi and Maskawa [17] for three generations of quarks to explain the observed CP violation. The 3×3 matrix called the Cabibbo-Kobayashi-

Maskawa (CKM) matrix transforms the mass eigenstates (d, s, b) into the weak eigenstates (d', s', b') as follows

$$\begin{bmatrix} d' \\ s' \\ b' \end{bmatrix} = \begin{bmatrix} V_{ud} & V_{us} & V_{ub} \\ V_{cd} & V_{cs} & V_{cb} \\ V_{td} & V_{ts} & V_{tb} \end{bmatrix} \begin{bmatrix} d \\ s \\ b \end{bmatrix}. \tag{2.2}$$

The completeness and orthonormality of quark basis states require the CKM matrix to be unitary. The matrix elements that reflect the coupling of the possible quark pair (*e.g.*, V_{ud} measures the coupling of u to d) can be experimentally determined, and thus the unitarity can be tested in principle for any columns or rows of the matrix with the unitarity condition of $\sum_j V_{ij}V_{jk}^* = \delta_{ik}$. The most precise result comes from the top-row sum where the up quark couples with the down, strange, and bottom quarks *i.e.*, $|V_{ud}|^2 + |V_{us}|^2 + |V_{ub}|^2$. The dominant term, V_{ud}, can be extracted from four different sources: nuclear superallowed Fermi β decays, neutron β decay, pion β decay, and β-decay of odd-mass mirror nuclei. The second term, V_{us}, is currently obtained from K-meson decays. The third term, V_{ub}, determined from B-meson decays, is too small to have any impact on the unitarity test. The current status of V_{ud} and the unitarity test of the CKM matrix are presented in Sec. II.E.

D. Nuclear β decay

Nuclear β-decay occurs when an electron or positron is emitted from a nucleus consisting of protons, Z, and neutrons, N. During this process, the total number of nucleons, $A = Z + N$, remains unchanged. Three different types of β decay in nuclei

can be characterized as follows:

$$A(Z,N) \longrightarrow A(Z+1,N-1) + e^- + \overline{\nu_e} \qquad \beta^- \text{ decay}$$
$$A(Z,N) \longrightarrow A(Z-1,N+1) + e^+ + \nu_e \qquad \beta^+ \text{ decay}$$
$$e^- + A(Z,N) \longrightarrow A(Z-1,N+1) + \nu_e \qquad \text{electron capture (EC).}$$

In the decay processes, the energy release, Q, can be expressed in terms of the mass difference between the parent and daughter nuclei:

$$Q_{\beta^-} = [m(Z,N) - m(Z+1,N-1)]c^2 \tag{2.3}$$
$$Q_{\beta^+} = [m(Z,N) - m(Z-1,N+1)]c^2 - 2m_e c^2 \tag{2.4}$$
$$Q_{EC} = [m(Z,N) - m(Z-1,N+1)]c^2, \tag{2.5}$$

where $m(Z,N)$ is the atomic mass of parent nucleus, $m(Z \pm 1, N \mp 1)$ is the mass of daughter nucleus, and m_e is the mass of the electron. For β^- decay to be possible, $m(Z,N)$ should be larger than $m(Z+1,N-1)$. Usually β^+ decay competes with the electron capture process as both decays result in the same daughter nucleus. However, the difference of $2m_e c^2$ (1.022 MeV) in Q-values between β^+ decay and electron capture determines whether both decay modes are energetically permitted. When the mass difference between parent and daughter nucleus is less than $2m_e c^2$, the transition decays solely by electron capture.

1. Selection rules

All β transitions are empirically classified into allowed and forbidden transitions. In this treatment, the nucleons are described non-relativistically. The emission of leptons for allowed decays are assumed to have zero orbital angular momentum ($L = 0$) relative to the nucleus. Since leptons do not carry any intrinsic orbital angular momentum, the only change in the angular momentum of the nucleus comes from

the spins of the electron and neutrino, each of which has the value of $S = \frac{1}{2}$. The emitted leptons can either couple their spins in anti-parallel ($S = 0$) or in parallel ($S = 1$). Accordingly, the total angular momentum, J, of the nucleus can change by 0 or 1. Decays with $S = 0$ are called Fermi transitions whereas those with $S = 1$ are called Gamow-Teller transitions. Allowed transitions, leading to Fermi and/or Gamow-Teller transitions, have the same parity between initial and final nuclear states. Transitions which can only proceed by $L > 0$ are referred to as forbidden, where the degree of forbiddeness (first forbidden, second forbidden, *etc*) refers to the L value ($L = 1$, $L = 2$, *etc*). The first forbidden transition ($L = 1$) involves a change of parity since the parity selection rule is $\pi_i\pi_f(-)^L = \text{even}$, where π_i and π_f are the parity of the initial and final states.

Similar selection rules can be established in terms of the isospin formalism as well. Protons and neutrons are indistinguishable if the nuclear force is assumed to be charge independent. Isospin is defined to describe this situation in analogous terms to the case of a spin-$\frac{1}{2}$ particle with two different substates. Protons and neutrons can be considered as two states of a single particle, the nucleon. For a nucleon with an isospin of $t = \frac{1}{2}$, the projection of isospin on the quantized axis, t_z, characterizes the proton state of $t_z = -\frac{1}{2}$ and the neutron state of $t_z = +\frac{1}{2}$, respectively. In a nucleus composed of Z protons and N neutrons, the z-projection of isospin, T_z, is defined as

$$T_z = \frac{N - Z}{2}, \tag{2.6}$$

and the total isospin, T, the sum of the individual nucleon isospins t, has a range

$$\frac{|N - Z|}{2} \leq T \leq \frac{N + Z}{2}. \tag{2.7}$$

Since the nuclear force energetically favors the states with the lowest isospin, usually the ground state of a nucleus is expected to have an isospin of $T = |T_z| = |\frac{N-Z}{2}|$ [18]

Table II. Selection rules for allowed transitions

Fermi transitions	
$J_f = J_i$	$(\Delta J = 0)$
$T_f = T_i \neq 0$	$(\Delta T = 0)$
$T_{zf} = T_{zi} \mp 1$	$(\Delta T_z = \pm 1)$
$\Delta\pi = 0$	no parity change
Gamow-Teller transitions	
$\Delta J = 0, 1$	(but $J_i = 0 \rightarrow J_f = 0$ forbidden)
$\Delta T = 0, \pm 1$	
$T_{zf} = T_{zi} \mp 1$	$(\Delta T_z = \pm 1)$
$\Delta\pi = 0$	no parity change

although for odd-odd $N = Z$ nuclei the ground state can be $T = T_z + 1 = 1$. In isospin space, the Fermi transition is restricted to $\Delta T = 0$ transitions between isobaric analogue states, where the only difference between parent and daughter states is the interchanged role of a proton and neutron. Gamow-Teller decay can occur when $\Delta T = 0, \pm 1$. The selection rules for allowed transitions are summarized in Table II.

Transitions from an initial state of $J_i^\pi = 0^+$ to a final state of $J_f^\pi = 0^+$ with the same isospin T are an especially important class known as superallowed transitions, a subclass of allowed β-decays. These transitions are pure-vector Fermi transitions and are nearly independent of the detailed structure of the nuclei involved. Superallowed β decays are all positron emitters.

2. The ft values

The measured strength of a β transition is expressed in terms of its ft value, where f is the statistical rate function, which depends on the proton number of the daughter nucleus and the measured total decay energy, Q_{EC}; t is the partial half-life which depends on the half-life, $t_{1/2}$, of the parent state and the branching ratio, R, for the transition of interest. For a superallowed $0^+ \longrightarrow 0^+$ transition between $T = 1$ analogue states, the ft value can be written as

$$ft = \frac{K}{G_V^2 \langle M_F \rangle^2}, \tag{2.8}$$

where $K/(\hbar c)^6 = 2\pi^3 \hbar \ln 2/(m_e c^2)^5 = 8120.2787(11) \times 10^{-10}\ GeV^{-4}s$ and G_V is the vector coupling constant for semileptonic weak interactions. The Fermi matrix element, $\langle M_F \rangle$, can be evaluated under the assumption that isospin is a good quantum number. The parent and daughter states are isospin analogue states in this case, and since the isospin ladder operator $\tau_\pm$ is the Fermi transition operator, $\langle M_F \rangle$ is given by

$$\begin{aligned} \langle M_F \rangle &= \langle JMT_f T_{zf} | \tau_\pm | JMT_i T_{zi} \rangle \\ &= \sqrt{T_i(T_i+1) - T_{zi} T_{zf}}, \end{aligned} \tag{2.9}$$

where i and f label the initial and final states, respectively. For $T = 1$ states, the transition matrix has the value of $\langle M_F \rangle = \sqrt{2}$.

From Eq. 2.8, it is clearly seen that the ft values for the superallowed $0^+ \longrightarrow 0^+$ β decays should be the same regardless of the nuclei involved, providing that G_V is a fundamental constant and, as indicated by the CVC hypothesis, is not renormalized to another value in the nuclear medium. In practice, however, the measured ft values are not truly constant because the presence of the Coulomb interaction between

charged particles destroys isospin symmetry and leads to isospin-symmetry breaking corrections. Radiative corrections also play an important role. With these small theoretical corrections for such effects, the corrected $\mathcal{F}t$ value is defined in the following form [2]

$$\mathcal{F}t \equiv ft(1+\delta_R^{'})(1+\delta_{NS}-\delta_C) = \frac{K}{2G_V^2(1+\Delta_R^V)}, \tag{2.10}$$

where $\delta_R^{'}$, δ_{NS}, and Δ_R^V are radiative corrections and δ_C is a correction for isospin-symmetry breaking. These theoretical corrections will be described in the next section. In particular, the method developed by Towner and Hardy [2, 19] is closely followed to discuss δ_C and δ_{NS}.

a. Radiative corrections, δ_R and Δ_R^V

For the unitarity test of the CKM matrix through the precision measurements of the superallowed β decays, it is important to consider various radiative processes, such as the emission of real photons (bremsstrahlung) and the exchange of virtual photons and Z-bosons, since radiative corrections are one of the largest contributors to the uncertainties. Radiative corrections can be categorized into a nucleus-dependent outer correction, δ_R, and a nucleus-independent inner correction, Δ_R^V. Recently, Marciano and Sirlin [20] reevaluated Δ_R^V with a better control of hadronic uncertainties, and substantially reduced its uncertainty by a factor of 2. The current value for the Δ_R^V [20] is

$$\Delta_R^V = (2.361 \pm 0.038)\% \tag{2.11}$$

The nucleus-dependent correction, δ_R, is separated into two parts:

$$\delta_R = \delta_R^{'} + \delta_{NS}. \tag{2.12}$$

The nuclear-structure independent term, $\delta_R^{'}$, is a function of the electron energy and the charge of the daughter nucleus Z while the nuclear-structure dependent term, δ_{NS}, is a second-order correction involving a weak axial-vector interaction. Although a transition between 0^+ states is purely vector, in second order a weak axial-vector interaction can combine with an axial-vector electromagnetic interaction to produce a vector interaction. It is possible that the axial-vector interaction may flip a nucleon spin and then a virtual photon emitted by the departing positron flips it back again. The whole process seems to be a pure vector interaction from the intrinsic spins point of view. However an axial-vector weak interaction was a carrier. Two interactions can occur on the same nucleon or on two separate nucleons. The computation of the latter depends on nuclear structure; the result is labeled δ_{NS}. A shell-model calculation is used to obtain δ_{NS}. More details can be found in Ref. [2, 19].

b. Isospin symmetry-breaking correction, δ_C

Since isospin is not a perfect symmetry in nuclei, the nuclear states are no longer the isospin analogue states and the value of the Fermi matrix element is reduced from its exact-symmetry limit. For the superallowed β decay, the Fermi matrix M_F is written as

$$|M_F|^2 = |M_F^0|^2(1 - \delta_C), \tag{2.13}$$

where M_F^0 is the exact-symmetry value given in Eq. 2.9 and δ_C is the correction to be evaluated.

The δ_C can be divided into two parts

$$\delta_C = \delta_{C1} + \delta_{C2}. \tag{2.14}$$

A correction to δ_{C1} arises from the configuration mixing among the 0^+ state wave func-

tions in the parent and daughter nuclei. In the method of Towner and Hardy [2, 19], the shell model is used to calculate δ_{C1}. An appropriate nucleon-nucleon interaction was selected to include the two-body Coulomb terms in the proton-proton part of the Hamiltonian, a 2% increase in $T = 1$ proton-neutron elements (justified by the charge dependence observed in nucleon-nucleon scattering data) and one-body elements determined from the single-particle energies of closed-core-plus-proton and -neutron nuclei. This evaluation was constrained by the reproduction of the measured b- and c-coefficients in the isobaric-multiplet mass equation that describes the multiplet involved in the superallowed transition.

The second term δ_{C2} is due to small differences in the single-particle neutron and proton radial wave functions. Since the protons are typically less bound than the neutrons, the tail of the wave function for protons is longer than that for neutrons, which results in the radial overlap integral being less than unity. The radial functions were determined to be the eigenfunctions of the Saxon-Woods potential whose strength or well depth was adjusted so that calculated eigenvalues matched the measured proton separation energy in the parent nucleus and the neutron separation energy in the daughter nucleus.

Although these calculated corrections are only of order of $\sim$1% [2], they are significant when compared to the present level of experimental precision. Consequently, it is important to establish the reliability of the calculations. Fortunately there is a powerful method for testing the reliability of the nuclear-structure-dependent correction terms, δ_C and δ_{NS}: Do they lead to consistent $\mathcal{F}t$ values for all measured transitions? The uncorrected ft values for the 13 most precisely measured transitions scatter over a range of nearly 2%, yet the corrected $\mathcal{F}t$ values must be statistically consistent with one another if the CVC hypothesis is to be satisfied. The requirement that CVC must be satisfied has been shown to be a sensitive test of the validity of

the calculated structure-dependent correction terms, a test that so far has only been successfully passed by the set of calculations that is based on the effective-interaction shell model combined with Saxon-Woods radial wave functions (SM-SW) [21].

E. Current status of world data

In 2009, a new critical survey of world data on superallowed $0^+ \longrightarrow 0^+$ beta decays was published [10]. Over 145 independent measurements for Q_{EC}, $t_{1/2}$, and R covering 20 superallowed transitions were considered to determine the experimental ft values and the fully corrected $\mathcal{F}t$ values leading to the precision tests of the CVC and the unitarity of CKM matrix. Typically, the experimental uncertainties from Q_{EC}, $t_{1/2}$, and R measurements were quoted at the limit of 0.005%, 0.03%, and 0.001%, respectively. The most precise results, from 13 superallowed transitions, ^{10}C, ^{14}O, ^{22}Mg, ^{26m}Al, ^{34}Cl, ^{34}Ar, ^{38m}K, ^{42}Sc, ^{46}V, ^{50}Mn, ^{54}Co, ^{62}Ga, and ^{74}Rb, formed a consistent set of $\mathcal{F}t$ values within statistical uncertainties, which verified the CVC hypothesis at the level of 1.3 $\times 10^{-4}$. The new average value of $\mathcal{F}t$ was obtained to be $\overline{\mathcal{F}t} = 3071.81 \pm 0.83$ s. This update of $\overline{\mathcal{F}t}$ impacted directly on the value of V_{ud} derived from the vector coupling constant, G_V, and the weak interaction coupling constant, G_F, determined from the purely leptonic muon decay. As $\overline{\mathcal{F}t}$ is inversely proportional to G_V^2 (see Eq. 2.10) and $V_{ud} = G_V/G_F$, the V_{ud} becomes

$$V_{ud}^2 = \frac{K}{2G_F^2(1+\Delta_R^V)\overline{\mathcal{F}t}}. \tag{2.15}$$

Combined with the recent improved calculations of Δ_R^V [20] and the Particle Data Group (PDG) value of $G_F/(\hbar c)^3 = (1.16637 \pm 0.00001) \times 10^{-5}\ GeV^{-2}$ [22], the value of V_{ud} from the superallowed $0^+ \longrightarrow 0^+$ beta decays was found to be

$$|V_{ud}| = 0.97425 \pm 0.00022\ [10]. \tag{2.16}$$

From three alternative methods, the values for V_{ud} are

$$|V_{ud}| = 0.9758(13)\ [1] \qquad \text{neutron } \beta \text{ decay} \tag{2.17}$$

$$|V_{ud}| = 0.9742(26)\ [1] \qquad \text{pion } \beta \text{ decay} \tag{2.18}$$

$$|V_{ud}| = 0.9719(17)\ [1] \qquad \beta\text{-decay of odd-mass mirror nuclei} \tag{2.19}$$

To date, superallowed β^+ emitters provide by far the most precise determination of V_{ud}. Although the other three methods have reported consistent values for V_{ud}, experimental difficulties have limited the precision of those measurements. For neutron β decay, the major obstacle is the 5.6 standard-deviation discrepancy between the two most precise measurements of the neutron lifetime [23, 24]. This problem demands new and more precise neutron-lifetime measurements to resolve the controversy. The separation between the axial-vector and vector contributions is also challenging for β-asymmetry experiments and correlation measurements on both neutron and mirror-nuclei β decay. In pion β decay, the beta decay channel is very weak ($\sim 10^{-8}$). With the best known values for V_{ud}, V_{us}, and V_{ub}, the unitarity test on the top row of the CKM matrix yields a result at the level of 0.06% precision:

$$|V_{ud}|^2 + |V_{us}|^2 + |V_{ub}|^2 = 0.99990 \pm 0.00060\ [1]. \tag{2.20}$$

This result confirms unitarity within tight limits.

CHAPTER III

EXPERIMENTAL SETUP AND PROCEDURES

The decay of the superallowed β^+ emitters ^{38}Ca and ^{46}V has been studied with the K500 superconducting cyclotron at the Cyclotron Institute. In these experiments, we produce very pure sources with the Momentum Achromat Recoil Spectrometer (MARS) [25], implant a measured number of ions into the aluminized mylar tape of our fast tape-transport system and move this source into a well-shielded counting location. There, the precise half-life is measured by using a 4π proportional gas counter or the branching ratio is determined with a plastic scintillator and 70% high-purity germanium detector (HPGe). A detailed description of our experimental setup and procedures is given in this chapter.

A. Production of isotopes

1. The Momentum Achromat Recoil Spectrometer

The Momentum Achromat Recoil Spectrometer (MARS) has been used for a broad range of nuclear physics studies *via* inverse kinematics reactions. Its good mass resolution and high efficiency are very effective features to produce a wide variety of pure secondary radioactive beams. The schematic layout of MARS is shown in Fig. 1. A primary beam obtained from the K500 superconducting cyclotron bombards a hydrogen-filled gas cell which is separated from the high-vacuum beam line by Havar entrance and exit windows. Degrader or stripper foils can be placed at the entrance and exit of the gas cell to tune the final beam energy and charge state. The cell is operated at liquid-nitrogen (LN2) temperature of around 77 K with constant pressure maintained at 2 atm.

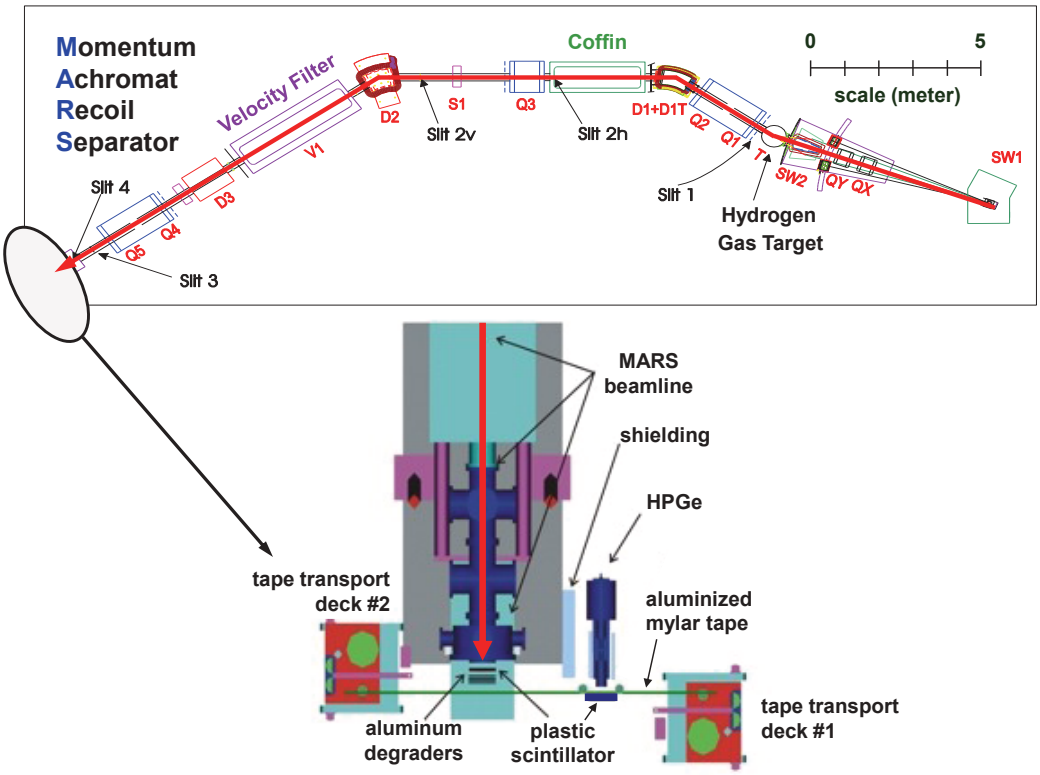

Fig. 1. Simplified experimental arrangement used in our branching-ratio measurement.

Reaction products are filtered into a secondary beam by undergoing two dispersive planes. By the quadrupole doublet magnet Q1-Q2 and the first dipole magnet D1, the maximum momentum dispersion is first obtained horizontally at the entrance to the quadrupole magnet Q3. The combination of the first three quadrupoles (Q1, Q2 and Q3) and first two dipoles (D1 and D2) produces an achromatic and nearly parallel beam into the velocity filter where the velocity dispersion occurs vertically as the second dispersion. The beam bent by the dipole D3 follows an q/m (charge-to-mass ratio) focus through the last quadrupole doublet Q4-Q5. A movable Faraday cup is located at the coffin to integrate the primary beam so that the production rate of a reaction can be determined.

There are four sets of slits along the beam line. Slits SL1 located right after

the gas target chamber determine the solid-angle acceptance. Horizontal selection slits SL2 in front of Q3 defines the momentum acceptance of the system. After the quadrupole doublet Q4-Q5, slits SL3 set the solid angle of the secondary beam. The last slits SL4 are used to select a particular value of q/m.

2. ^{38}Ca

We obtained ^{38}Ca via the inverse-kinematics reaction, $p(^{39}\mathrm{K}, 2n)^{38}\mathrm{Ca}$. A 30$A$ MeV ^{39}K beam bombarded a 2-atm hydrogen gas target cooled to liquid nitrogen temperature. The fully stripped ^{38}Ca ejectiles were separated by their charge-to-mass ratio q/m with MARS. Initially working with a low-current primary beam, we inserted a 1-mm-thick 16-strip position-sensitive silicon detector (PSSD) at the focal plane of MARS. This detector was used first for the identification of secondary reaction products, then for control of the selection and focus of ^{38}Ca in the center of the beam line. Fig. 2 shows the energy deposited in the detector versus position in the focal plane. This gives a clear indication of any nearby reaction products that could potentially contribute as impurities to our extracted beam. In this case, only ^{38}Ca and a very weak contribution from ^{35}Ar appear; $^{38}\mathrm{K}^{m}$ is far off scale to the left and can be completely excluded. With the focal-plane acceptance slits set to a width of 8.4 mm (dashed lines in Fig. 2), the ^{35}Ar contribution to the total extracted beam was determined to be 0.6%.

After the tune-up procedures had been completed, we removed the PSSD and increased the primary beam intensity. The ^{38}Ca beam from the acceptance slits then exited the vacuum system through a 51-μm-thick Kapton window, passed through a 0.3-mm-thick BC404 scintillator, used to count the ions, and then through a stack of aluminum degraders, finally stopping in the 76-μm-thick aluminized Mylar tape of a fast tape-transport system. The combination of q/m selectivity in MARS and

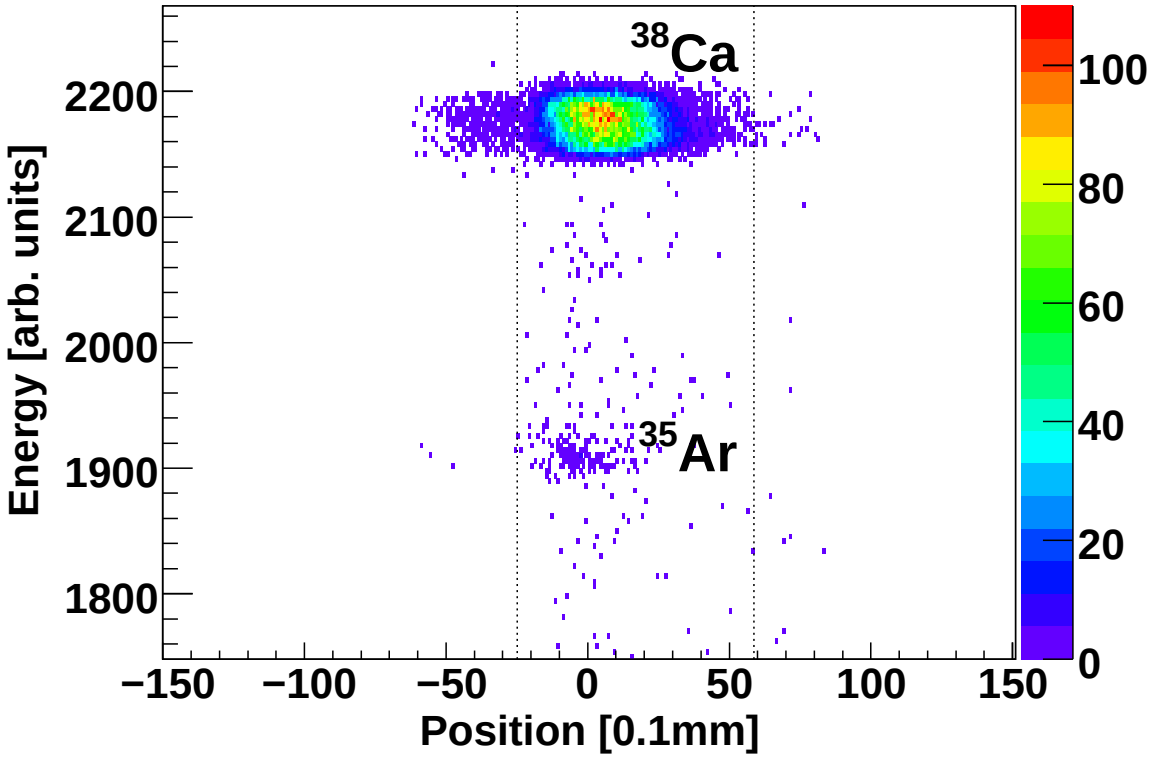

Fig. 2. Deposited energy versus position as recorded in the PSSD at the MARS focal plane. This result was obtained after the spectrometer had been tuned for ^{38}Ca. The dashed lines show the position of the extraction slits, 8.4 mm apart, which we used during these measurements. Note that the tail to the left of the main ^{38}Ca peak is an artifact caused by incomplete charge collection in strip detector. From such spectra recorded periodically during our experiment, we determined that the extracted ^{38}Ca beam included a 0.6% contribution from ^{35}Ar.

range separation in the degraders provided implanted samples that we determined to be better than 99.6% pure (see Sec. IV.C). We checked the composition of the beam exiting MARS on a daily basis by reinserting the PSSD at the MARS focal plane. No appreciable changes were observed.

3. ^{46}V

After making concerted efforts over several years to develop a useful titanium beam from our ECR ion-source, we employed a metal foil, 94% enriched in ^{47}Ti, as source material and successfully obtained a 32A MeV ^{47}Ti beam with up to 50 nA of current from the K500 superconducting cyclotron. Directing this beam into a hydrogen gas target, we produced ^{46}V via the inverse-kinematics reaction ^{1}H(^{47}Ti, 2n)^{46}V. The hydrogen gas cell had 4-μm-thick Havar entrance and exit windows. To increase the gas density and the yield of reaction products, it was operated at liquid-nitrogen temperature and at 2-atm pressure. The fully-stripped reaction products exiting the target cell entered MARS, where they were separated according to their charge-to-mass ratio q/m, with ^{46}V being selected in the focal plane.

Initially working with a low-current primary beam, we inserted the 1-mm-thick 16-strip position-sensitive silicon detector (PSSD) at the focal plane of MARS. This detector was used first for the identification of secondary reaction products, then for control of the selection and focus of ^{46}V in the center of the beam line. As shown in Fig. 3, in addition to ^{46}V, there were four reaction products, ^{42}Sc ($t_{1/2}$ = 680.72 ms), ^{43}Sc ($t_{1/2}$ = 3.891 h), ^{44}Ti ($t_{1/2}$ = 60.0 y) and ^{45}Ti ($t_{1/2}$ = 3.083 h), that appeared between the extraction slits and were thus weak contaminants in the extracted ^{46}V beam. The presence of ^{44,45}Ti and ^{43}Sc was not problematic since their half-lives are more than four orders of magnitude longer than 423-ms ^{46}V. Our only concern was ^{42}Sc, another superallowed β-emitter with a rather similar half-life to that of

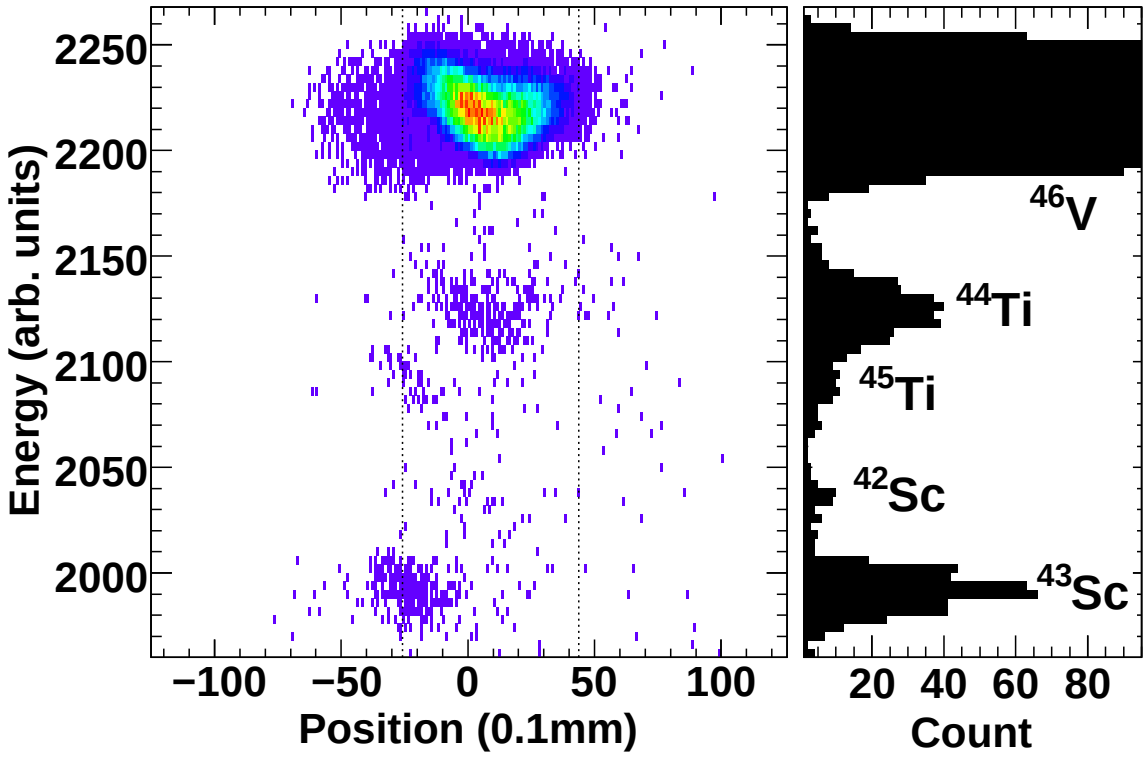

Fig. 3. Deposited energy versus position as recorded in the PSSD at the MARS focal plane. This result was obtained after the spectrometer had been tuned for ^{46}V. The dashed lines show the position of the extraction slits, 7 mm apart, which we used during these measurements. Note that the tail to the left of the main ^{46}V peak is an artifact caused by incomplete charge collection in the strip detector. From such spectra recorded periodically during our experiment, we determined that the extracted ^{46}V beam included a 0.12% contribution from ^{42}Sc.

^{46}V. With the focal-plane acceptance slits of MARS set to a width of 7 mm, the total extracted beam contained 0.12% of ^{42}Sc nuclei. The composition of the beam exiting MARS was checked on a daily basis during our half-life measurement: on each occasion we reinserted the PSSD at the MARS focal plane and acquired a spectrum equivalent to the one shown in Fig. 3. There were no appreciable changes observed in the extracted beam composition at any time.

B. Fast tape-transport system

The fast tape-transport system is used at the end of the MARS focal plane to move the sources collected on the aluminized mylar tape into the well-shielded counting location. It consists of two reels, reservoir reel and take-up reel, which are mounted independently on two separate decks. Each tape deck has its own vacuum buffer and controls, and the height of the deck is adjustable by motor drive. The tape-transport system operates entirely in air for use with the relatively energetic radioactive beams extracted from the MARS.

The tape leaves a reservoir reel by being engaged by a pinch roller located on the take-up reel deck; it is guided through the position of collection just beyond the MARS focal plane, enters the counting station, and is wound on the take-up reel. Air bearings are strategically installed along this horizontal path to ensure that the tape moves smoothly. Two brakes are located on both sides of the counting location to stop the tape promptly and to stretch it tightly in front of the detectors. The distance that the tape moves is determined by the pre-set time between the engagement of the pinch roller and the closing of the brakes. When clear leader is detected at the end of the tape, the tape rewinds automatically and cycling starts automatically after the rewind is complete. The times for the collect/move/count periods can be manually

set by thumbwheels on an electronics control panel on one of the tape decks or be remotely controlled by computer-generated signals input to the controller.

C. Half-life measurements of ^{38}Ca and ^{46}V

1. 4 π proportional gas counter and electronics

The 4π proportional gas counter consists of two separate gas cells machined from copper, which, when assembled, have a 0.25-mm slot between them, through which the Mylar transport-tape passes. Each cell contains a 13-μm-diameter gold-plated tungsten wire along the central axis, which is connected through insulators to positive high voltage. On the side facing the tape, each cell has a 3.7-cm-diameter entrance window sealed with 1.5-μm-thick Havar foil. Methane at $\sim$1 atm flowed continuously through each gas cell. Methane offers adequate gas gain for detecting positrons and is quite insensitive to γ rays.

Signals from the gas counter were fed into a preamplifier and fast timing-filter amplifier set to high gain ($\times$500). After the first stage of amplification in the amplifier, we have inserted a Schottky diode to clip large pulses that would otherwise have saturated the amplifier and delayed its recovery. The clipped and amplified signals were then input to a discriminator with very low threshold (150-250 mV). The discriminator output was then split and passed to two fixed-width, nonextending gate generators, which imposed different dominant dead times in two parallel multiscaled data streams. The time increment per channel for the multichannel scalars was externally controlled by a function generator accurate to 0.01 ppm. The two different dead times (gate widths) were continuously monitored on-line to an accuracy of $\pm$5 ns. Having these two data streams allowed us to test that our dead-time corrected results were independent of the actual dead time of the circuit. A more detailed

description of our electronic arrangement can be found in Ref. [26].

Before our half-life measurement, the safe operating range for the detector bias voltage was determined with a ^{90}Sr/^{90}Y β source, which had been prepared on a sample length of transport tape. Positioning this β source in the slot between the two halves of the detector—exactly where the radioactive sample is delivered on-line— we measured the counting rate as a function of the applied detector voltage at the three different thresholds used in our half-life measurements (150, 200 and 250 mV). Initially, as the applied voltage is raised the count-rate also rises since the increasing gas gain leads to more primary ionizing β events triggering the discriminator. However, at approximately 2600 volts—the exact value depends on the threshold setting—a "plateau" is reached, and the count rate remains nearly unchanged for the next 200-300 volts increase in the bias voltage. At higher voltages still, there is a second rapid rise in the count rate as spurious pulses increasingly trigger the discriminator. During our half-life measurement, the detector was always operated in the plateau region as determined in advance with the ^{90}Sr/^{90}Y source. Under these conditions, the detector efficiency was close to 100% and was essentially independent of count rate.

2. Special precautions

As the experiment for the half-life of ^{38}Ca and ^{46}V was aimed at the highest possible precision, many tests for systematic effects were made and special precautions taken during the measurements themselves:

(i) Every experiment was subdivided into many separate runs, differing only in their particular combination of detection parameters: dominant deadtime, detector bias, and discrimination threshold. For the ^{38}Ca half-life measurement, we used combinations of four different dead times (3, 4, 6, and 8 μs), three detector

biases (2600, 2700, and 2800 V) and three discriminator thresholds (150, 200, and 250 mV). The half-life of ^{46}V was measured with combinations of four different dead times (3, 4, 6, and 8 μs), two detector biases (2650 and 2750) and three discriminator thresholds (150, 200, and 250 mV). A separate analysis of each individual run allowed us to test for systematic effects that could contribute to the uncertainty in the final result.

(ii) Since each ^{38}Ca decay produces a ^{38}K^m daughter that also decays, the ratio of the parent-to-daughter activities depends on the time-dependence of the rate at which ^{38}Ca accumulates in the tape during the collection period. The number of ions registered in the scintillator located just in front of the aluminum degraders was recorded as a function of time with each cycle, and the results were used in our analysis.

(iii) Our tape-transport system is quite consistent in placing the collected source within $\pm$3 mm of the center of the detector. However, it is a mechanical system and some exceptions occur. We monitored its performance closely by separately recording the number of nuclei detected in the BC404 scintillator at the exit from MARS during the collection period of each cycle, and the number of positrons detected in the gas counter during the subsequent count period. The ratio of the latter to the former is a sensitive measure of whether the source was seriously misplaced in the proportional counter. We used this ratio as one of the data-selection criteria in our later analysis.

(iv) A background measurement was made in which all conditions were identical to those of a normal run except that the tape motion was disabled. The background rate at our shielded counting location was $\sim$ 1 count/s, which is 3-4 orders of magnitude lower than the initial count rate for each collected sample and is

consistent with the background level observed in normal runs.

(v) In one run, the decay spectrum was measured with long collect/detect times to probe for unanticipated longer-lived impurities. For ^{38}Ca activities were collected for 4 s and counted for 40 s in repeated cycles. Apart from ^{38}Ca, only the decay of ^{35}Ar ($t_{1/2} = 1775.4$ ms) was evident. For ^{46}V nothing was found from the decay spectrum recorded with 300 s collect and detect times.

3. Test of fitting procedures

A new fitting program was developed under the framework of ROOT [27] to find the parameters of a three-component (parent-daughter plus background) decay curve that best describes the experimental data. The recipe [28] we closely followed was based on a direct application of the maximum likelihood method to the Poisson distribution. The fit was performed with the maximum-likelihood constraints defined as follows:

$$\frac{\partial}{\partial p^{(j)}} \sum_{i=1}^{500} \overline{W}(i)[\overline{D}(i) - \overline{Y}(i)]^2 \;\; = \;\; 0 \tag{3.1}$$

where $\overline{Y}$(i) is a fitted function; $\overline{D}$(i) is the sum of dead-time-corrected data; and $\overline{W}$(i) is the average weight scaled by the ratio of the fitted function to the sum of dead-time-corrected data. For more details, the reader is referred to Ref [28]. To evaluate the fitted functions and variances for each iteration, the MINUIT [29] algorithm was used based on the parameters determined from the preceding iteration. The fitting routine was terminated when the estimated distance to the minimum was less than 0.0001%.

This new analysis program was successfully tested with ten different sets of simulated data, mimicking the real data obtained from an experiment. With 10,000 particles randomly generated in 500 channels for each cycle, a total of 1000 cycles

Table III. Summary of input parameters for simulating two-component decay curve.

input	values
collect time	1.0 s
move time	0.2 s
count time	5.0 s
dead time	3.0 μs
background rate	1 event/s, 10 events/s
half-life (parent/daughter)	0.450 s / 0.925 s

were created. All input parameters for the simulation are summarized in Table III, and Fig. 4 shows the fit results obtained from the new analysis package. The fitted results for the simulated data, 0.4498(2) s and 0.4500(2) s, agree perfectly with the actual half-life, 0.4500 s, used in generating the data. This verifies our analysis procedures.

4. Exploratory measurements

a. ^{38}Ca

Before we made our final successful measurement, we conducted two studies of the half-life of ^{38}Ca, the first an exploratory one and the second a higher-statistics one that suffered from an unusually unstable – and high (up to $\sim$3%) – contamination from ^{35}Ar ($t_{1/2}$ = 1.77 s) in the extracted ^{38}Ca beam at the focal plane of MARS. Since the difference in range between ^{38}Ca and ^{35}Ar is less than half the thickness of our mylar collection tape, our positioning of the stopped ^{38}Ca ions mid-way through the tape resulted in the simultaneous deposit of some ^{35}Ar near the back of the tape.

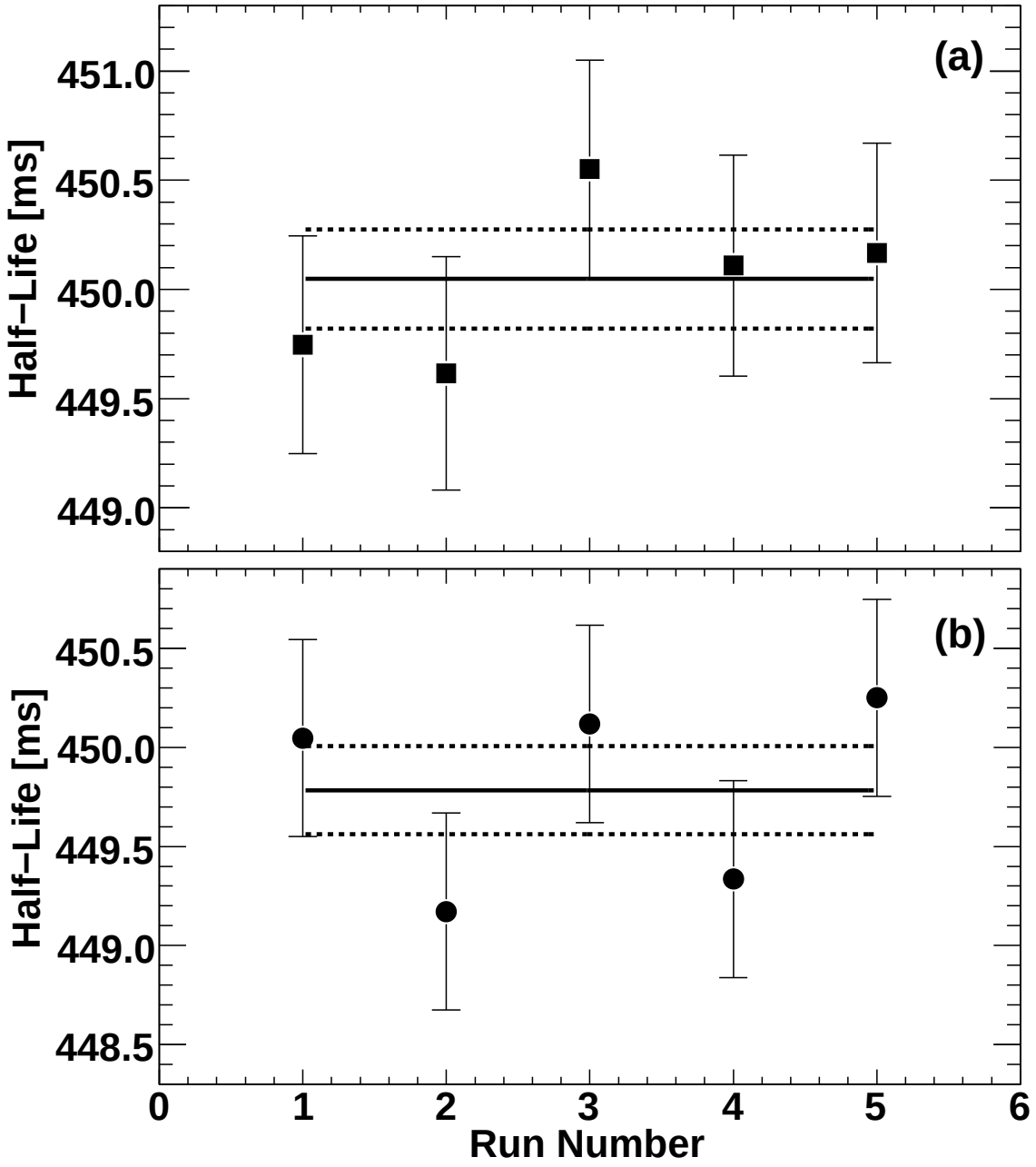

Fig. 4. Fitted half-lives for the simulated two-component decays with two different background rates: (a) The background rate of 10 events/s was used to generate all five sets of data. The average value for the fitted half-lives from these five sets is 0.4500(2) s with $\chi^2/ndf = 2.1/4$. (b) The background rate of 1 event/s was used to generate all five sets of data. The average value for the fitted half-lives from these five sets is 0.4498(2) s with $\chi^2/ndf = 3.9/4$.

Although the contribution of ^{35}Ar could be accounted for when we extracted the half-life of ^{38}Ca, we decided to repeat the measurement because the precision of our result could be further improved by better control of the impurities and by optimized positioning of the collected sample in the tape.

b. ^{46}V

We tried the first experiment on October 2008 after two production tests. It turned out that the production of a ^{47}Ti beam at 32A MeV was a real challenge for the accelerator. For most of the time, the beam current was less than 10 nA, which barely met the minimum β-particle counting rate required from a statistics point of view. However, we were able to obtain data for only one third of the seven-day requested beam time. With repeated cycles of 1 s/0.192 s/10 s collect/move/count times, over 30 million β events were recorded for one set of dominant dead times. Unfortunately, the useful beam time was not sufficient for us to check for systematic errors. However, our result for the half-life was consistent with the average of all previous measurements, 422.50(11) ms [10].

Another five-day run followed in December 2008 to improve the overall statistics of the data and to check for any possible systematic errors. Unfortunately, our analysis revealed a small systematic effect on half-life in this measurement. To achieve a higher gain in excess of 500, we had replaced our preamplifier with a quad bipolar amplifier that allowed for cascading of input channels. Although previous off-line tests with a ^{90}Sr/^{90}Y β source revealed no problems, the fast pulses generated on-line by radioactive ^{46}V samples caused significant signal overshoot and a baseline drift. Consequently, we restored the original preamplifier in the electronic chain for the final half-life measurement of ^{46}V.

D. Branching-ratio measurement of ^{38}Ca

1. The β-γ coincidence method and detectors

The decay of ^{38}Ca offers a superallowed branch, which feeds the isomeric state of its daughter ^{38}K, as well as competing Gamow-Teller branches to higher excited states that release γ rays. Since the branching ratio is a measure of the partial transition probability to a particular final state as a fraction of the total from a specific initial state, this decay scheme forces our experiment to focus on the β-delayed γ rays, requiring that the absolute γ-ray intensities be determined.

The β-γ coincidence technique is a very powerful way to achieve this goal [30]. The principle of the method is to measure the simultaneous emission of a β-particle and a γ-ray with two detectors within a defined resolving time. This only occurs when a nucleus de-excites to a particular final state by emitting a γ ray following a β-decay branch. The important information obtained from the coincidence measurement is not only the time connection between two coincident events but also the energy distribution of the two radiations correlated in time. For this reason, the β-γ coincidence technique gives us the great advantage of eliminating the γ-ray room background, which has no correlated β, and also allows us to clean the γ spectrum of counts connected with unwanted β events.

In our experimental configuration at the counting location, a 1-mm thick BC404 plastic scintillator for β particles was placed 2 mm from the mylar collection tape. The desirable properties of this β detector are energy proportionality, fast time response and insensitivity to γ radiation, making it suitable to measure β singles as well as β events in coincidence with γ rays. The response of our β detector has been characterized as a function of energy with conversion-electron sources and Monte Carlo calculations [31, 32]. The high-purity germanium (HPGe) detector for γ rays

was positioned on the opposite side of the tape from the plastic β-detector. It is a coaxial n-type detector with an active volume of 280 cm^3 and has a efficiency of 70% for 1.33-MeV γ-rays relative to a $3'' \times 3''$ NaI(T1) crystal [33]. The distance from the radioactive source collected on tape to our HPGe detector was 15 cm, which is the optimum to obtain sufficient statistics in a reasonable period of accelerator operation without introducing a large coincidence summing effect. Our HPGe detector has been meticulously calibrated at 15 cm using 13 individual sources from 10 different radionuclides: ^{48}Cr, ^{60}Co, ^{88}Y, ^{108}Ag^m, ^{109}Cd, ^{120}Sb^m, ^{133}Ba, ^{134}Cs, ^{137}Cs and ^{180}Hf^m. The absolute efficiency of our HPGe detector is known to 0.2% in the energy range from 50 to 1400 keV, and to 0.4% from 1400 keV to 3500 keV [33, 34, 35].

2. Data acquisition

Fig. 5 is a schematic diagram of the data acquisition system that has been developed at the Cyclotron Institute of Texas A&M University for the precise branching-ratio measurement. The system hardware includes a CAMAC controller with SCSI capability, three types of converters (Analog-to-Digital Converter (ADC), EG&G Ortec, model AD413A; Charge(Q)-to-Digital Converter (QDC), LeCroy, model 4300B; Time-to-Digital Converter (TDC), LeCroy, model 3377), a FERA driver, two dual port FERA/CAMAC buffer memories and a PC with the Windows NT operating system. Based on FERA (Fast Encoding and Readout ADC) electronics and KmaxNT software [36], the key feature of this system is a significant reduction in the dead time associated with data flow after digital conversion. To achieve the best in timing and energy resolution for a coincidence measurement, the circuit split the signals from each detector into two branches, one associated with time and the other with energy, processed them separately, and then combined the results (see Fig. 5). We recorded time-tagged β-γ coincidence data event by event. The β and γ-ray energies, the co-

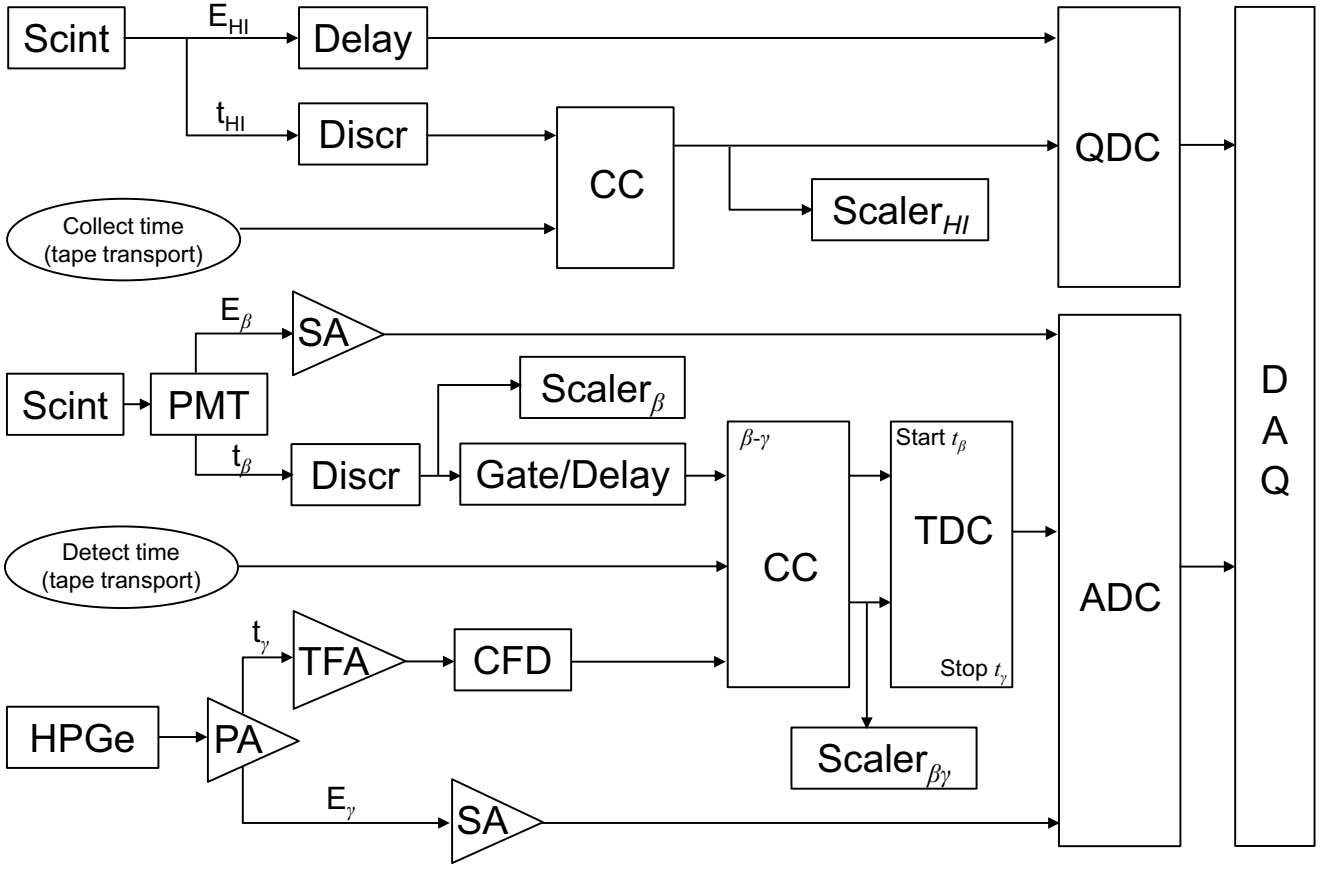

Fig. 5. Schematic diagram of the data acquisition system used to measure the branching ratio of ^{38}Ca.

incidence time between them, and the time of the event after the beginning of the cycle were all recorded, as was the total number of β-singles events for each cycle. The same discriminator signal used for scaling was also used in establishing the β-γ coincidences.

3. Exploratory measurement

An exploratory measurement of the branching ratio for ^{38}Ca was performed on which separated ^{38}Ca was produced by MARS with the same reaction and primary beam energy used in the half-life measurement for ^{38}Ca. By repeating a *collect-move-count* cycle of 1.5-0.180-1.5 s, we measured time-tagged β-γ coincidence events with the 1-mm-thick plastic scintillator for β particles and our 70% HPGe detector for the γ rays. In a five-day run, approximately, 2.5 million β-γ coincidence events were recorded together with around 100 million β singles. Although the overall statistics needed to be improved for our targeted precision, the preliminary analysis of these data showed that the measured relative γ-ray intensities were consistent with the values previously known from Ref. [37].

After this measurement, improvements were made in the experimental equipment, which allowed us to measure the electronic dead times and the source-to-detector distance cycle by cycle. The former was achieved by pulser signals from a constant frequency pulse generator measured in coincidence with gating signals from β-singles events, γ-singles events, and β-γ coincidence events. Because the total number of generated pulser events is known, the loss factor is simply the ratio of recorded to generated pulser events. The addition of a laser triangulation device into our system also allowed us to determine the source-to-detector distance accurate to $\pm$0.1 mm in the range from 9 to 19 cm [38]. With this upgraded system, every detection cycle is now tagged with its own source-to-detector distance. This increases

the precision we can achieve in a branching-ratio measurement to the limit defined by the precision of the absolute efficiency of the γ-ray detector. These improvements were implemented into a second measurement of the branching-ratio of ^{38}Ca.

CHAPTER IV

PRECISE HALF-LIFE OF ^{38}Ca

As seen in Fig. 6, the decay of ^{38}Ca feeds ^{38}K^m, which is also a superallowed emitter with a half-life that is 2.1 times longer than that of ^{38}Ca. To achieve high precision under these circumstances we needed to produce high-purity ^{38}Ca samples, with no initial contribution from ^{38}K^m (see Sec. III.A.2); and use the specialized analysis techniques that we developed previously for our studies of other linked parent-daughter decays, those of ^{34}Ar [26] and ^{26}Si [39]. Our approach will be described briefly in the following sections, but for further detail the reader is referred to those two earlier publications.

After we had collected ^{38}Ca for 1 s, the cyclotron beam was interrupted and the collected sample moved in 198 ms to the center of a 4π proportional gas counter located in a well-shielded area about 90 cm away. The decay positrons detected from the gas counter were multiscaled for 15 s into two separate 500-channel time spectra, each corresponding to a different pre-set dominant dead-time. Note that the 15-s count period is equivalent to 34 half-lives of ^{38}Ca or 16 half-lives of its daughter ^{38}K^m. These collect/move/count cycles were controlled by the tape-transport system, and their timing was continuously monitored on-line by the data-acquisition computer. The cycles were repeated until the desired overall statistics had been achieved.

For this measurement, over 125 million β events were obtained from 11,271 cycles divided into 32 separate runs. Before analyzing the data, we first removed any cycles that had fewer than 500 β-particles detected by the gas counter, which indicated little—or no—primary beam from the cyclotron during the collection period. We then excluded cycles that had an anomalously low ratio of recorded β-particles to implanted ^{38}Ca ions as observed in the scintillator. A low ratio is indicative of faulty

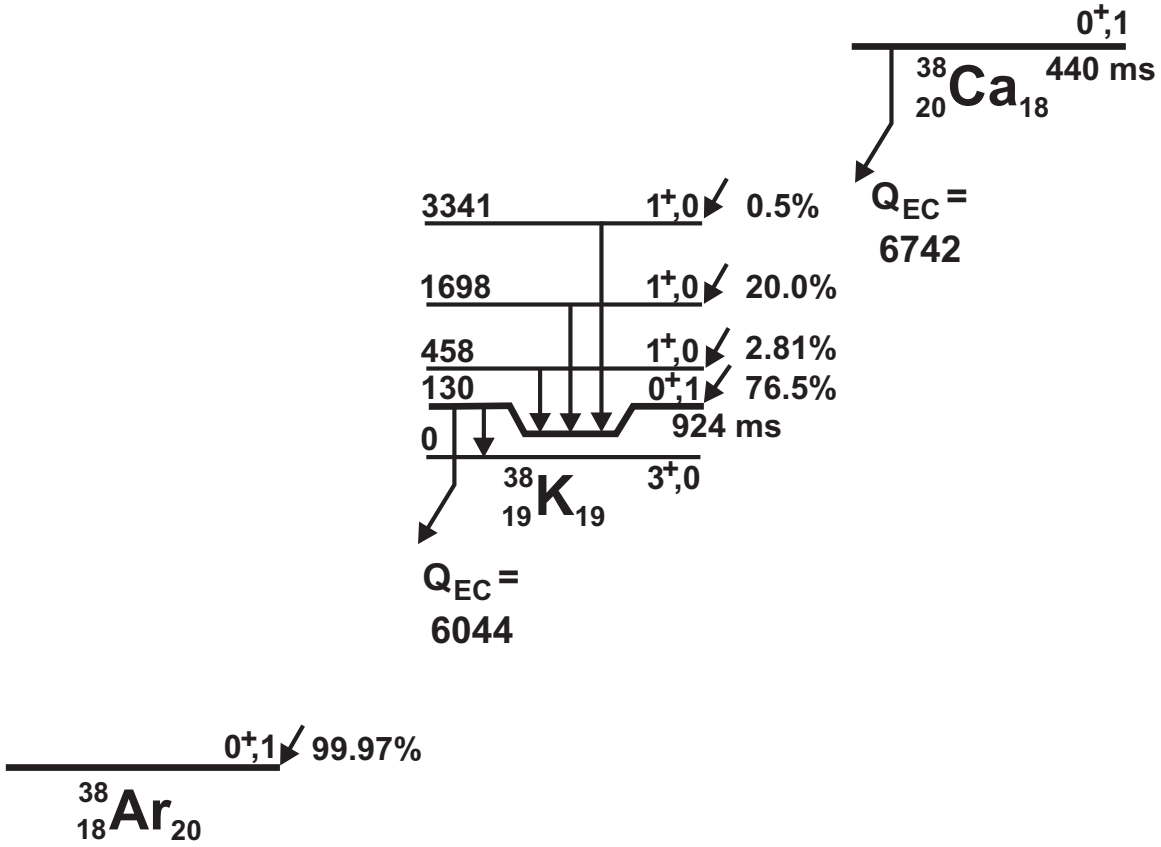

Fig. 6. Decay schemes of ^{38}Ca and ^{38}K^m showing only those features relevant to their superallowed β decays. All energies are in keV, and the Q_{EC} values shown are for the superallowed branches. The data are adopted from Ref. [40], in which the measured relative β-branching ratios for ^{38}Ca were normalized to a calculated value for the superallowed branch. Three weak β branches from ^{38}Ca to higher excited states have been omitted: their branching ratios total $<$0.2%. Note that there is a 0.03% γ-decay branch from the isomeric state ^{38}K^m to the ^{38}K ground state [41].

tape motion leading to a misplaced sample in the gas detector. As a result of these pre-selections, approximately 11% of the cycles were rejected from all 32 runs. The remaining data were corrected cycle-by-cycle for dead-time losses based on the method described in Ref. [28]. The final decay spectrum for each run was then obtained from the sum of the dead-time corrected decay spectra from all accepted cycles in that run.

The total time-decay spectrum obtained from the combined runs is presented in Fig. 7, where we also show the separate contributions from the ^{38}Ca parent and ^{38}K^m daughter. This breakdown into components is based upon our final analysis and is presented here simply to illustrate how the parent-daughter decay curve, which combines two rather similar half-lives, tends to mask the parent half-life even though the parent activity dominates at the start of the counting period.

A. Parent-daughter connection

The total positron activity from the combined decays of ^{38}Ca and its daughter ^{38}K^m can be described by the coupled decay equations:

$$\Lambda_{total} = C_1 e^{-\lambda_1 t} + C_2 e^{-\lambda_2 t}, \tag{4.1}$$

with

$$\begin{aligned} C_1 &= N_1 \epsilon_2 \lambda_1 \left(\frac{\epsilon_1}{\epsilon_2} - \frac{\lambda_2}{\lambda_1 - \lambda_2} \right) \\ C_2 &= N_1 \epsilon_2 \lambda_2 \left(\frac{N_2}{N_1} + \frac{\lambda_1}{\lambda_1 - \lambda_2} \right) \end{aligned} \tag{4.2}$$

where t is the time elapsed after the end of the collection period; $N_{1,2}$ are the numbers of ^{38}Ca and ^{38}K^m nuclei present in the sample at $t = 0$; $\epsilon_{1,2}$ are the experimental efficiencies for detecting the positrons from the respective decays; and $\lambda_{1,2}$ are the corresponding decay constants.

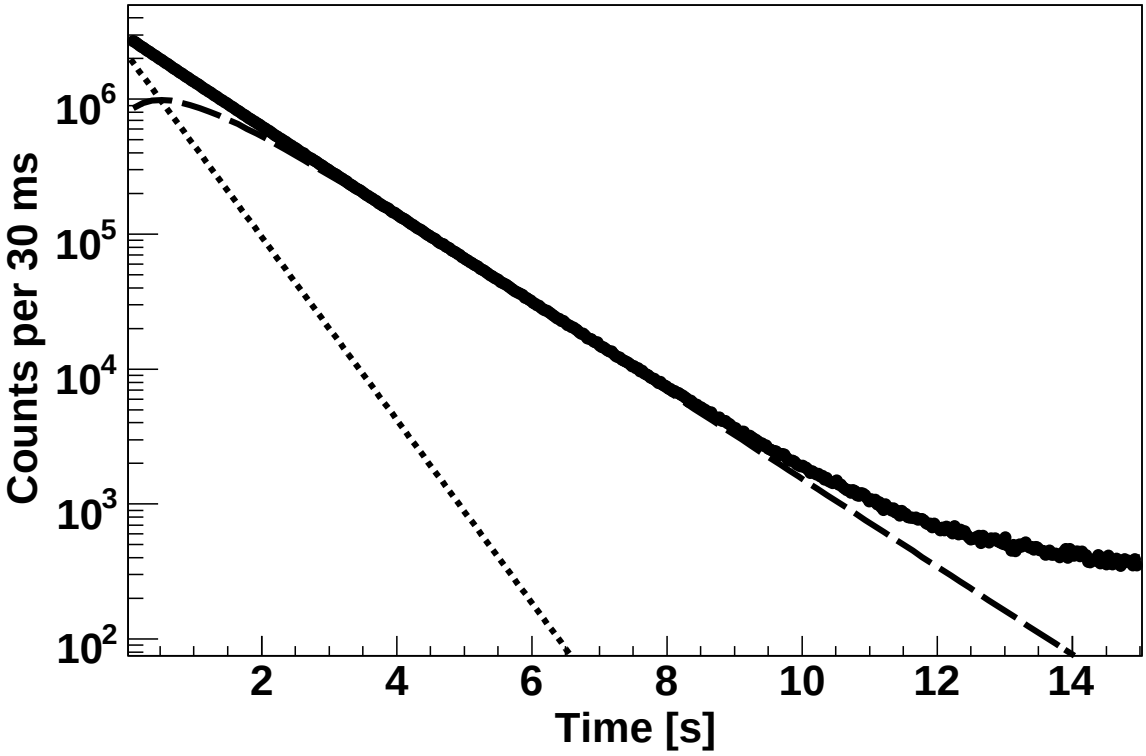

Fig. 7. Measured time-decay spectrum for the total of all data obtained from the β^+ decay of ^{38}Ca and its daughter ^{38}K^m. The dotted/dashed lines represent the derived ^{38}Ca/^{38}K^m contributions.

When $\lambda_1 = 2\lambda_2$ (and $\epsilon_1 = \epsilon_2$) the coefficient C_1 vanishes, leaving a single exponential term having the decay constant of the daughter. This is very nearly the case for the decays of ^{38}Ca and ^{38}K^m, which have decay constants that are related by a factor of 2.1. Consequently, for our measurements, the coefficient C_1 is more than a factor of 10 smaller than C_2. The impact is clearly evident in Fig. 7 where the growth and decay of the daughter activity almost completely masks the decay of the parent. This imposes a serious limitation on the precision that can be obtained from a free fit to the data. Even with λ_2 fixed at its known value, C_1, C_2, and λ_1 (as well as the constant background) must all be determined independently, which leads to a λ_1 with very large uncertainty.

This deficiency can be overcome by application of the technique we developed and used in our previous measurements of the half-lives of ^{34}Ar [26] and ^{26}Si [39], which have similar coupled decays. The key element is to fix the ratio of C_2/C_1 so that the number of adjustable parameters in the fit is reduced to three (including background). To achieve this we must determine the two ratios, N_2/N_1 and ϵ_1/ϵ_2, from our experimental parameters.

If the ^{38}Ca-sample collection rate were exactly constant, it would be a simple matter to calculate the N_2/N_1 ratio from the production of ^{38}K^m (via ^{38}Ca decay) over the collection period. Instead of relying on approximate constancy, though, we recorded as a function of time the number of ^{38}Ca ions detected by the scintillator at the exit of MARS for each individual cycle. As shown in Fig. 8, there is a considerable variation in the collection rate over the first half of each collection period, caused by local heating and a concomitant drop in gas density along the path of the primary beam. Although the fan-assisted recovery to steady-state conditions is relatively fast, the initial variation is enough to make a change in the ratio N_2/N_1. We also found that the size of the variation depended on the primary beam intensity, thus

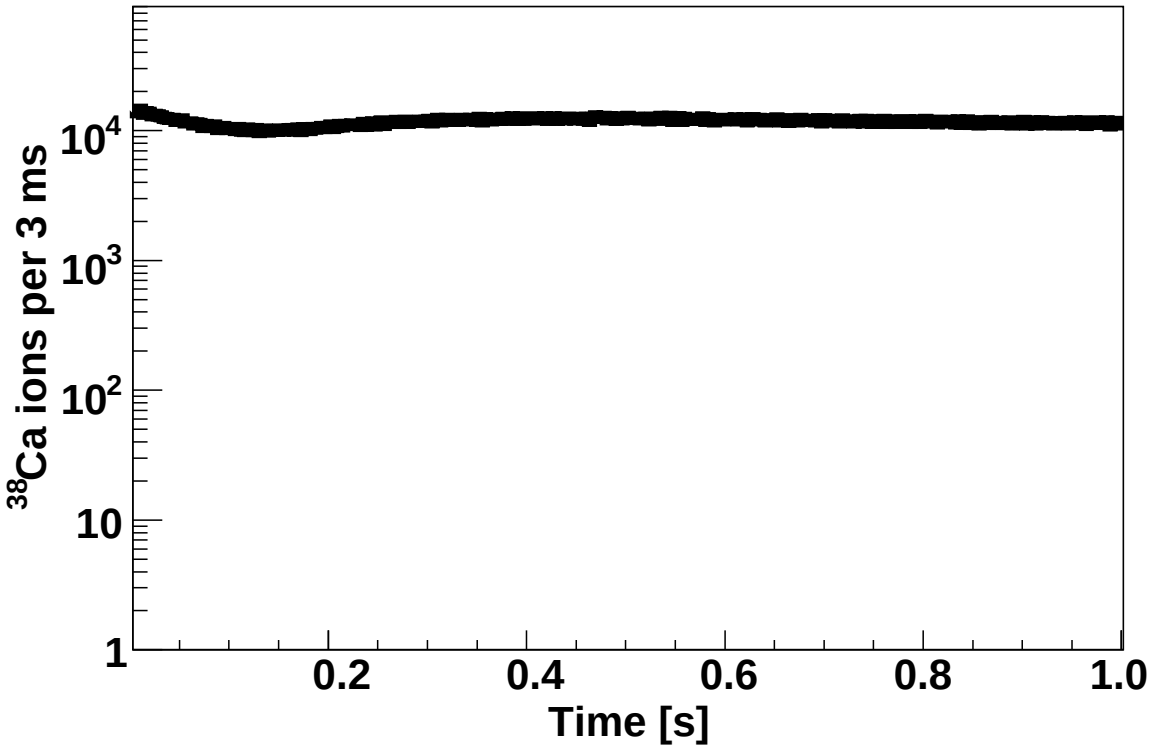

Fig. 8. Typical time-profile of the collected ^{38}Ca beam measured over the course of one run. The initial drop in intensity is generated by the decrease in local density of the hydrogen in the target cell as the primary beam heats the gas around its path. A fan located inside the gas-target mitigates the effect and ensures a rapid transition to stable conditions.

potentially changing the beam-profile from one cycle to another. However, with the collection-rate profile recorded, we could accurately determine the N_2/N_1 ratio for each cycle by obtaining the decay-production of ^{38}K^m from a numerical integration that incorporated the measured ^{38}Ca collection rate.

B. Parent-daughter relative efficiencies

For the coupled decays of ^{38}Ca and ^{38}K^m, it might easily be assumed that the efficiency ratio, ϵ_1/ϵ_2, equals unity since both activities were observed with identical geometry, a

very low electronic threshold and nearly 100% overall efficiency. However, there is also a threshold energy arising from the fact that low-energy positrons are stopped in the aluminized Mylar transport-tape (half-thickness, 38 μm) and in the Havar windows of the gas counter (1.5 μm thick), never reaching the active volume of the detector. The impact of this effective threshold on the efficiency ratio becomes significant when the end-points and/or shapes of the parent and daughter β spectra are significantly different from one another [39].

Fig. 9(a) presents calculated β spectra for ^{38}Ca and ^{38}K^m, with end-point energies of 5590 keV and 5022 keV respectively. The Gamow-Teller branches are included along with the superallowed branch for the ^{38}Ca spectrum; only the superallowed branch contributes to the decay of ^{38}K^m. In principle, for two such decays with different end-points, a low-energy cutoff removes a different fraction from each decay, leading to different effective efficiencies for detecting them. In practice, for the ^{38}Ca and ^{38}K^m decays, the lower energy Gamow Teller branches contributing to the former alter its spectrum shape enough that a small low-energy cutoff has nearly the same effect on both decays.

To evaluate the exact effect of the cutoff we modeled our exact tape/window/detector geometry within the Monte Carlo code EGSnrc (version V4-r2-3-0) [42] and calculated the overall system efficiency as a function of positron energy. The result is shown in Fig. 9(b). Because the decay positrons are emitted isotropically, their paths through the tape and window cover a range of lengths, resulting in a low-energy cutoff that is not sharp, as is evident in the figure. We convoluted the Monte Carlo result with each of the two β^+ spectra in Fig. 9(a) to obtain our overall efficiencies for detecting the parent and the daughter activities. The deduced efficiency ratio was $\epsilon_1/\epsilon_2 = 1.00042(5)$, where we have also incorporated the fact that ^{38}K^m has a 0.033(4)% γ-decay branch that competes with the superallowed decay branch [41].

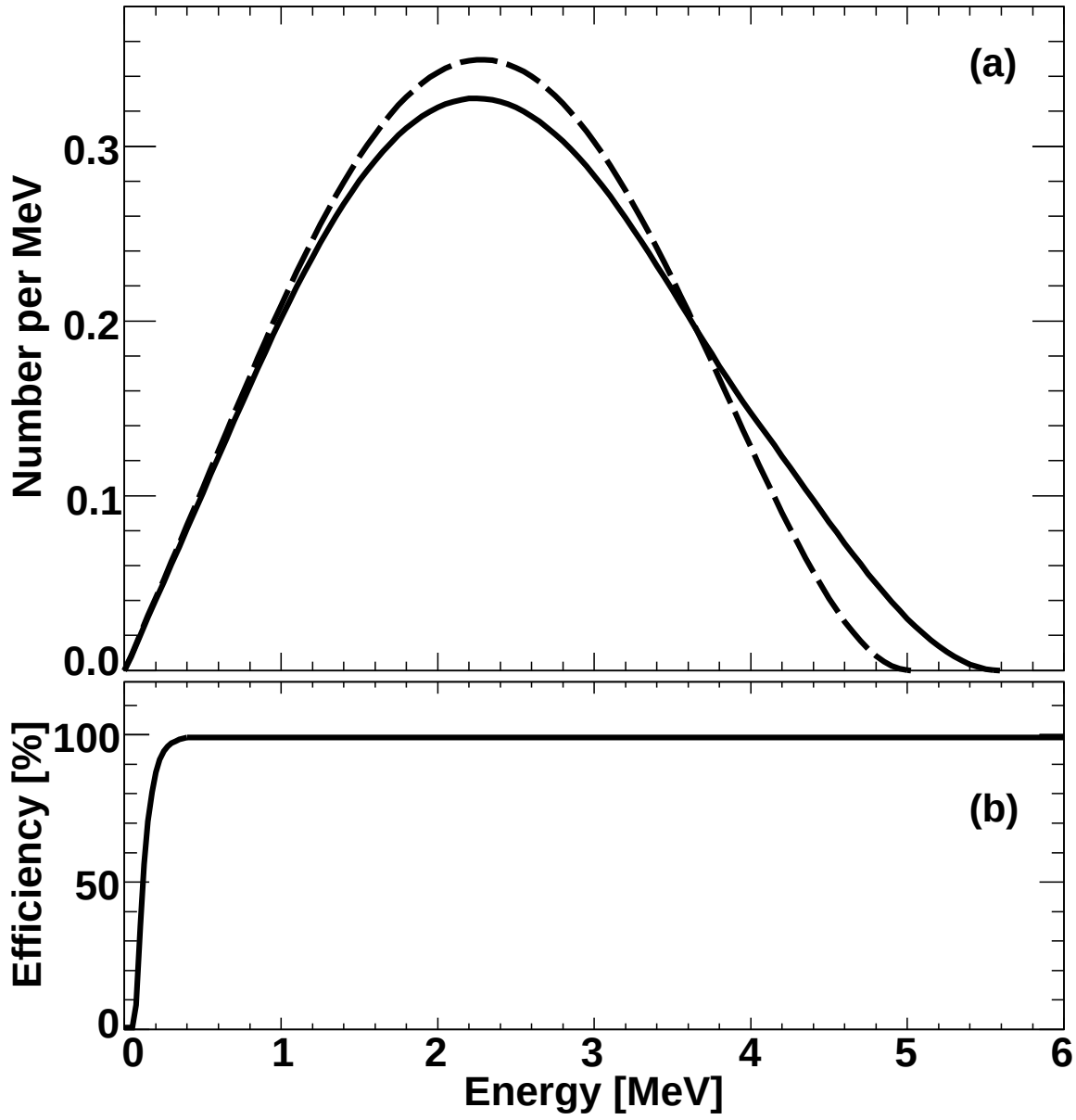

Fig. 9. (a) Calculated β^+ energy spectra for ^{38}Ca (solid curve) and ^{38}K^m (dashed curve), each normalized to unity. The former includes the Gamow-Teller branches to 1^+ states as well as the superallowed branch to the 0^+ isomer; the latter is a pure superallowed decay (see Fig. 6 for both decay schemes). (b) System efficiency for detecting positrons due to the effects of the aluminized Mylar tape and the Havar windows of the detector gas cells. The curve is the result of a Monte Carlo calculation with the EGSnrc code.

The uncertainty we quote on our efficiency ratio arises mostly from the uncertainty on the $^{38}K^{m}$ γ-decay branch but also from our assigning a $\pm 10\%$ relative uncertainty on the calculated ranges. This result for the efficiency ratio was used in the analysis of all runs.

C. Sample impurity

Based on the spectrum of reaction products identified at the MARS focal plane (see Fig. 2), we determined that ^{35}Ar ($t_{1/2}$ = 1775.4 ms) was present in our extracted beam with an intensity of 0.6% relative to that of ^{38}Ca. However, the amount of ^{35}Ar actually collected in the Mylar transport tape could be reduced further because ^{35}Ar loses slightly less energy than ^{38}Ca in traversing the aluminum degraders. With careful adjustment, we could retain virtually all the ^{38}Ca nuclei in the transport tape while letting at least some of the ^{35}Ar nuclei pass all the way through the tape.

To set this up, at the beginning of the experiment we measured the amount of ^{38}Ca activity collected in the tape as a function of degrader thickness. This allowed us to determine the depth distribution of ^{38}Ca in the tape and to verify that its spread in depth corresponded to the momentum spread as set by the momentum slits in MARS. Based on our measurement we could also determine the thickness of aluminum degraders required to place the collected ^{38}Ca activity exactly midway through the tape. The experimentally determined degrader thickness to achieve this was very close to the thickness we had calculated with the SRIM code [43]. This result verified the reliability of the code and gave us confidence to use it to determine the depth distribution of ^{35}Ar relative to that of ^{38}Ca. Unfortunately the code indicated that, with the stopped ^{38}Ca nuclei located mid-way through the Mylar tape, the ^{35}Ar would still be entirely in the tape as well, albeit nearer the back of it.

Accordingly, for our half-life measurements we reduced the thickness of aluminum degraders so as to deposit the ^{38}Ca at the back of the tape. A representation of the situation is given in Fig. 10. The depth distribution shown for ^{38}Ca was derived from our measurement of activity versus degrader thickness, and the implantation depth of ^{35}Ar relative to ^{38}Ca was the result of the SRIM calculation. Even with the ^{38}Ca nuclei implanted as deep as possible in the tape, the figure shows that approximately 75% of the ^{35}Ar nuclei in the beam extracted from MARS remained in the collection tape. Based on the relative intensities measured in the MARS focal plane (see Sec. III.A.2), this corresponds to an ^{35}Ar/^{38}Ca ratio of 0.45% in the collected samples. Unfortunately this cannot be considered a very precise result: an increase of only 3 μm in the depth of the implanted ions relative to the edge of the tape in Fig. 10 would change the ratio to 0.35%. We therefore sought a more precise method to determine the ^{35}Ar contribution.

To this end, we turned to the decay spectrum obtained with longer collect and count times (see item (v) in Sec. III.C.2). Because the half-life of ^{35}Ar is four times that of ^{38}Ca, a longer collect time ensured that the contribution of ^{35}Ar to our collected samples would be enhanced, and a longer count time made us more sensitive to its decay. As expected, in addition to ^{38}Ca, the decay of ^{35}Ar was clearly identifiable in the measured decay spectrum. No other impurities were found. We then fit the spectrum with four components: ^{38}Ca, ^{38}K^m, ^{35}Ar, and a constant background. The half-lives of ^{35}Ar and ^{38}K^m were fixed at 1775.4 ms [26] and 924.33 ms [10] respectively. The half-life of ^{38}Ca was also fixed for each fit, but we performed a number of fits with its half-life fixed to different values between 442 and 445 ms. This range was greater than the range of half-life values we obtained from an analysis of the short collect-and-count-time data (see following section), in which we considered ^{35}Ar impurity levels from 0.2% to 0.6%, the maximum possible. The impurity level obtained from

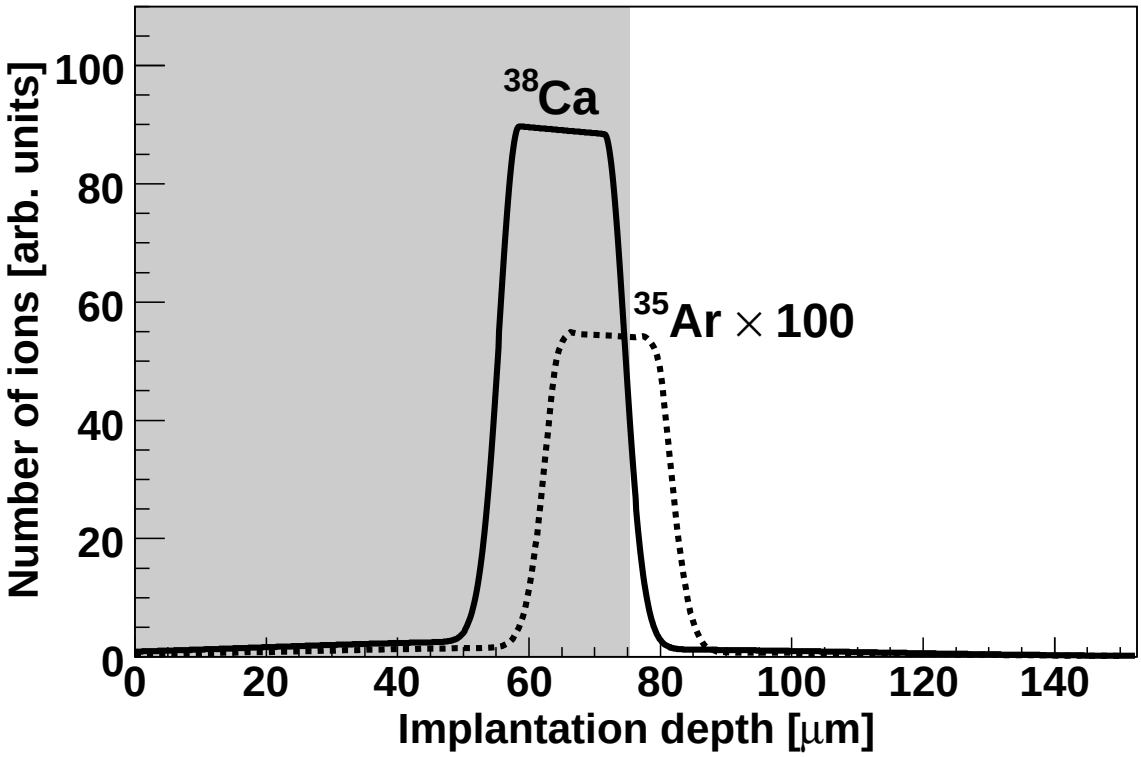

Fig. 10. The calculated implantation profiles of ^{38}Ca (solid line) and ^{35}Ar (dashed line) in and beyond the Mylar tape, under the conditions applying to our half-life measurements. The beams enter from the left. The shaded region corresponds to the actual thickness of our collection tape: all ions within the shaded region are collected in our sample; all others are not.

the fits to the long collect-and-count-time data turned out to be very insensitive to the half-life assumed for ^{38}Ca, allowing us to determine the ^{35}Ar/^{38}Ca ratio to be 0.36(5)% at the beginning of the collection period. This is the value we subsequently used for our final analysis of the short collect-and-count-time data.

D. Time decay analysis

Data from 32 separate runs were fitted with the linked parent-daughter decay equations presented in Sec. IV.A, to which were added terms incorporating the ^{35}Ar impurity and a constant background. The half-life of ^{38}K^m was fixed at its known value of 924.33 ms [10] and the ratio of its initial activity to that of ^{38}Ca was obtained for each run from numerical integration of the measured ^{38}Ca beam profile as a function of time in that run (see Sec. IV.A and Fig. 8). The efficiency ratio ϵ_1/ϵ_2 was fixed at 1.00042, the value established in Sec. IV.B. Finally, the ^{35}Ar half-life was also set to its known value of 1775.4 ms [26] and its initial relative activity was set to 0.36%, the value determined in Sec. IV.C.

Because each run was obtained under a different combination of detecting conditions, we could test for systematic effects by comparing the individually fitted half-lives of ^{38}Ca obtained from each run. As displayed in Fig. 11 the half-life results showed no dependence on either the applied bias voltages or the discriminator threshold settings. Although not illustrated, the results were also independent of the four different dominant dead times that were imposed in different runs. A further test, sensitive to the possible presence of undetected short-lived impurities or counting-rate dependent effects, is illustrated in Fig. 12. We removed data from the first 150 ms of the counting period and refitted the remaining data; then we removed an additional 150 ms of data and refitted again. We continued this procedure until 900 ms of data

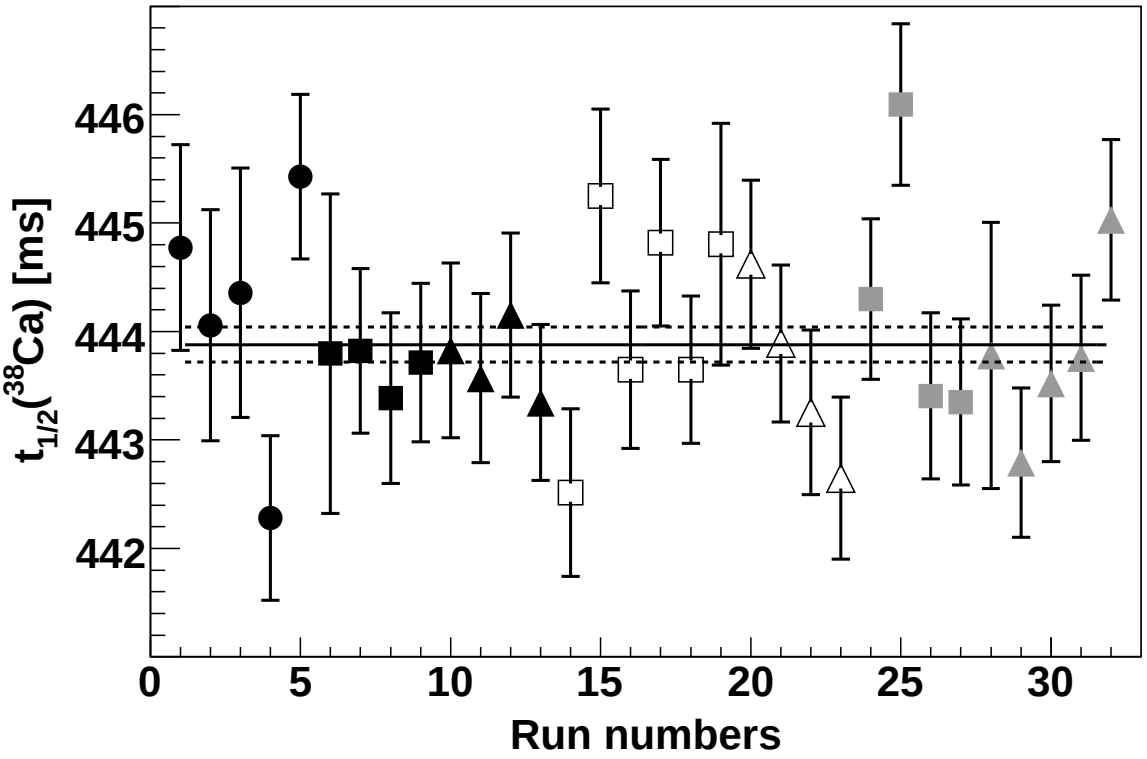

Fig. 11. Test for possible systematic bias in the ^{38}Ca half-life measurement due to discriminator threshold or detector voltage. Black/open/grey symbols represent the three discriminator settings, 150 mV/200 mV/250 mV; the three detector biases, 2600 V, 2700 V and 2800 V, are represented by the symbol shapes ◯, □ and △, respectively. The average value for the half-life is 443.88(16) ms (statistical uncertainty only) with $\chi^2/ndf = 39/31$. The average value appears as the solid line, with dashed lines as uncertainty limits.

had been removed. The figure demonstrates that the half-lives extracted under these conditions were consistent with one another within statistical uncertainties.

With these possible systematic effects eliminated as significant factors, our result for the ^{38}Ca half-life is determined to be $t_{1/2}(^{38}\mathrm{Ca}) = 443.88$ ms, with a statistical uncertainty of ± 0.16 ms. The normalized χ^2 of this average is 1.26, and the statistical uncertainty just quoted already includes multiplication by the square root of the normalized χ^2.

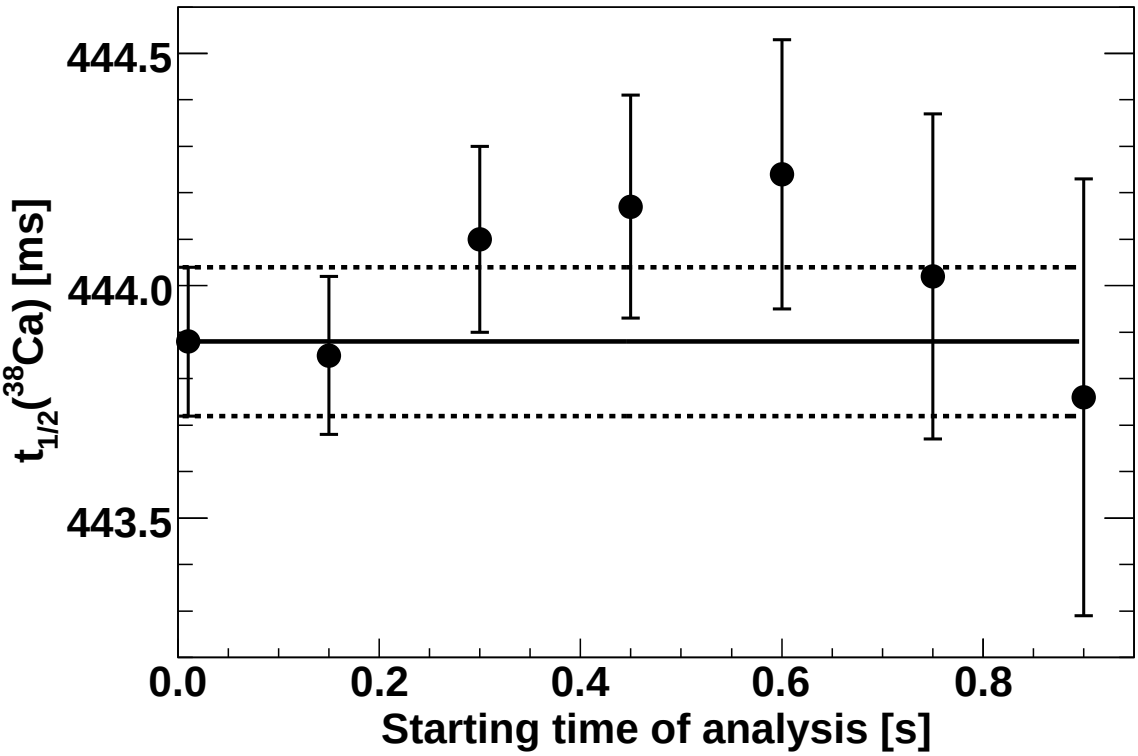

Fig. 12. Test for possible systematic bias in the ^{38}Ca half-life measurement caused by short-lived impurities or by rate-dependent counting losses that we have not accounted for. Each point is the result of a separate fit to the data; the abscissa for each point represents the time period at the beginning of the counting cycle for which the data were omitted from that particular fit. The solid and dashed lines correspond to the average half-life value and uncertainties given in Fig. 11.

Table IV. Uncertainty budget for the ^{38}Ca half-life measurement.

Source	Uncertainty (ms)
statistics	0.16
sample impurity (^{35}Ar)	0.23
$t_{1/2}(^{38}\mathrm{K}^m)$	0.22
efficiency ratio, ϵ_1/ϵ_2	0.01
Total	0.36
^{38}Ca half-life result (ms)	443.88(36)

E. Uncertainty budget

Naturally, other factors beyond counting statistics contribute to the overall uncertainty. We itemize the ones we are aware of in Table IV. The largest contribution comes from the uncertainty in the intensity of the ^{35}Ar impurity in the sample (see Sec. IV.C). The second largest is due to the uncertainty in the $^{38}\mathrm{K}^m$ half-life. Because we are dealing with a coupled parent-daughter decay, the fitted half-life obtained for the parent (^{38}Ca) depends strongly on the half-life used for the daughter ($^{38}\mathrm{K}^m$) in the fitting process. The value we used, 924.33(27) ms, was taken from the most recent review of superallowed β decays [10] and is the average of the six previous measurements quoted with better than $\sim$0.1% precision. The final contribution to our error budget is the one associated with the different efficiencies for detecting parent and daughter activities; it is very small because the ratio itself is so close to unity that it plays only a very minor role for this particular pair of decays. Our final result for the half-life of ^{38}Ca is 443.88(36) ms.

F. Comparison with previous results

Four out of the five previous measurements of the ^{38}Ca half-life were made before 1980 and with quoted uncertainties more than thirty times larger than ours: 470(20) ms [44], 439(12) ms [45], 450(70) ms [46] and 430(12) ms [47]. These were each obtained by observation and analysis of the decay of β-delayed γ-rays from the daughter, ^{38}K. The first result lies about one-and-a-half of its error bar away from our quoted half-life; the other three agree well within their error bars. There is a much more recent measured value, 443.8(19) ms [48], which was obtained in a similar manner to ours, from a measurement of the decay positrons in a gas counter; in their case, though, sample purity was achieved by collecting the ^{38}Ca first in a Penning trap. Our half-life result agrees well with theirs but with an uncertainty five times smaller.

CHAPTER V

PRECISE HALF-LIFE OF ^{46}V

A sample was collected in the tape for a fixed time – either 0.3 s or 0.5 s – after which the cyclotron beam was interrupted and the activity moved in 180 ms to 4π proportional gas counter at the counting location about 90 cm away. The length of the collection period was chosen to obtain an initial β-particle counting rate of between 5000 and 10000 particles/s; it was altered when necessary to compensate for changes in the primary beam intensity. The 4π proportional gas counter and associated electronics have already been described in Sec. III.C.1. In all, over 65 million β events were recorded from 14422 cycles divided into 16 runs. To illustrate the overall quality of the data, we present in Fig. 13 the total time-decay spectrum obtained by combining all the runs.

Before analysis we pre-selected the data based on two criteria. First, a cycle was rejected if the total number of β-particles detected by the gas counter was less than 500, indicating that there had been little or no primary beam from the cyclotron during the collection period. With the rather difficult ^{47}Ti beam this occurred quite often so approximately 9% of the total cycles from all 16 runs were eliminated by this criterion. The second criterion we used to exclude cycles was the measured ratio of detected β-particles to implanted ^{46}V ions as observed in the BC404 scintillator. For each run we restricted the ratio to being between 90 and 100% of the maximum value obtained for that run; this ensured that the ^{46}V sample had been centrally located in the detector. We have already shown this to be a safe range for the ratio [39] but, to be doubly sure, we checked it again with this measurement: we found that enlarging the accepted range by a further 10% had no appreciable affect on the extracted half-life. With the 90-100% criterion applied to the ratio, another $\sim$8% of the total cycles were

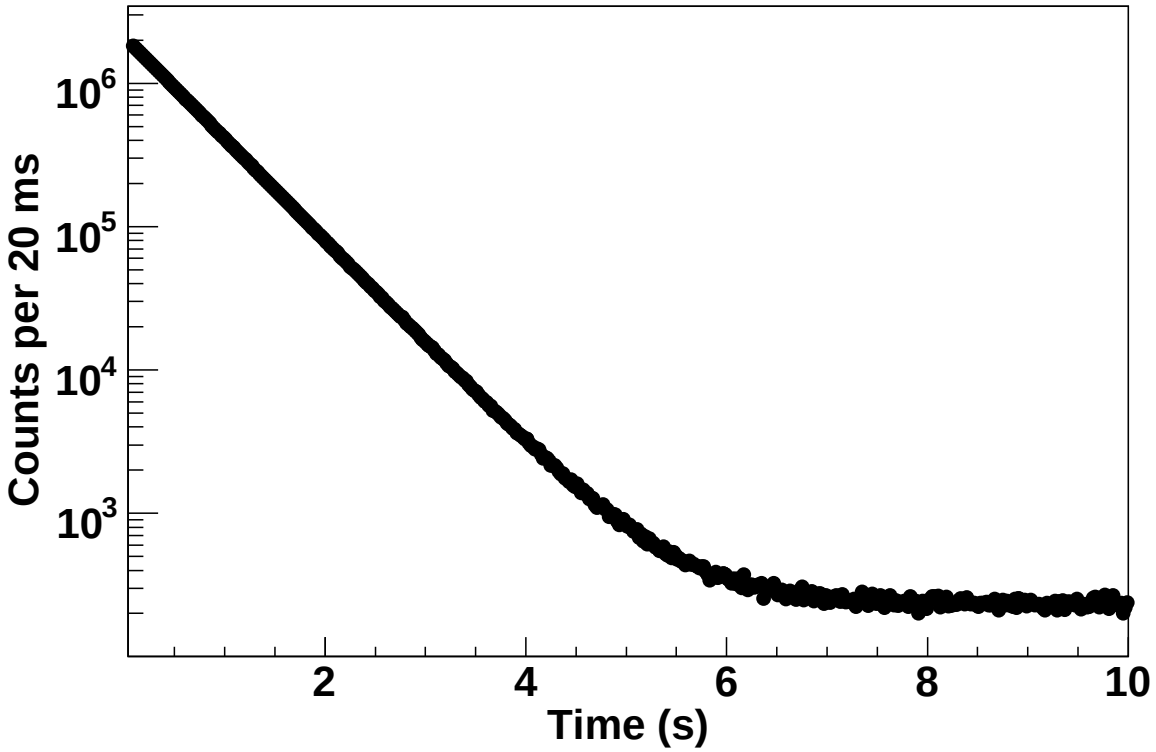

Fig. 13. Measured time-decay spectrum for the total of all data obtained from the β^+ decay of ^{46}V.

rejected from all 16 runs. The remaining data were then corrected cycle-by-cycle for dead-time losses, based on the method described in Ref. [28]. The final decay spectrum for each run was then obtained from the sum of the dead-time corrected decay spectra for all accepted cycles in that run.

A. Sample impurity

As explained earlier in Sec. III.A.3, ^{42}Sc is the only impurity in the beam with the potential to affect our half-life measurement. Other weak impurities seen in the MARS focal plane have half-lives much too long to be of any concern. We confirmed this conclusion by the decay spectrum taken with 300-s collect/detect times, in which no impurities with intermediate half-lives were detected.

Before the ^{46}V half-life measurement began, we took special precautions to reduce the effect of the 0.12% ^{42}Sc contaminant in the ^{46}V beam exiting from MARS. These were based on the fact that the ^{42}Sc ions have a different range in the aluminum absorbers than do the ^{46}V ions. To be able to make good use of this fact, we measured the amount of ^{46}V activity collected in the Mylar tape as a function of the thickness of aluminum degraders as we changed the degrader thickness from 57.15 μm to 133.35 μm in increments of 6.35 μm. This allowed us to determine the thickness of aluminum degraders required to place the collected ^{46}V activity exactly midway through the tape. The thickness so determined turned out to be very close to the thickness calculated with the code SRIM [43] and confirmed the reliability of the code in this application. We then used SRIM to determine the difference between the range of ^{42}Sc and that of ^{46}V, finding the former to be longer by about half the thickness of the Mylar tape. Thus, by depositing the collected ^{46}V samples near the back of the Mylar tape we could ensure that ^{42}Sc passed entirely through the tape. This virtually

eliminated any contribution from ^{42}Sc to our measured decay spectra.

To be more quantitative, we show as the solid line in Fig. 14 a simplified functional form for the implantation depth distribution of ^{46}V, which is consistent with the results of our scan of ^{46}V activity versus degrader thickness and with the known momentum spread as set by the momentum slits in MARS. We have then reproduced the shape of this empirical depth distribution as a dashed line to represent the distribution of ^{42}Sc. The difference in depth between the two was taken from a calculation with the SRIM code [43] and the relative magnitude was set at 0.12%, the amount we determined from our measurement with the PSSD in the MARS focal plane (see Sec. III.A.3). Although it is too small to be visible in the figure, our detailed scan of ^{46}V activity versus degrader thickness showed evidence of a very weak tail, amounting to $\sim$1% of the total, extending to the left of the depth distribution. We take this result to be a good gauge of the upper limit for how many ^{42}Sc nuclei could have been retained in the collection tape. With this approach we can then conclude that the ^{42}Sc/^{46}V ratio in the collected samples was less than 0.0015%, a result that makes negligible any contribution from ^{42}Sc to our extracted half-life for ^{46}V.

We also used a second independent method to search for any evidence of ^{42}Sc activity by examining the recorded time-decay spectra. We fitted each spectrum from the 16 individual runs with a function including two exponentials, one each for the decays of ^{46}V and ^{42}Sc, together with a constant background. In the first fit, we set the initial ^{42}Sc/^{46}V ratio of intensities to the 0.0015% value just obtained; set the half-life of ^{42}Sc to its world-average value, 680.72 ms [10]; and extracted a half-life for ^{46}V. Then we refitted the same 16 spectra with the initial ^{42}Sc/^{46}V ratio as the adjustable parameter. In this case, the half-life of ^{42}Sc was again set to its world-average value but the ^{46}V half-life was fixed at a range of values around the average value obtained from the first fit. We found that the ^{42}Sc/^{46}V ratio obtained from the

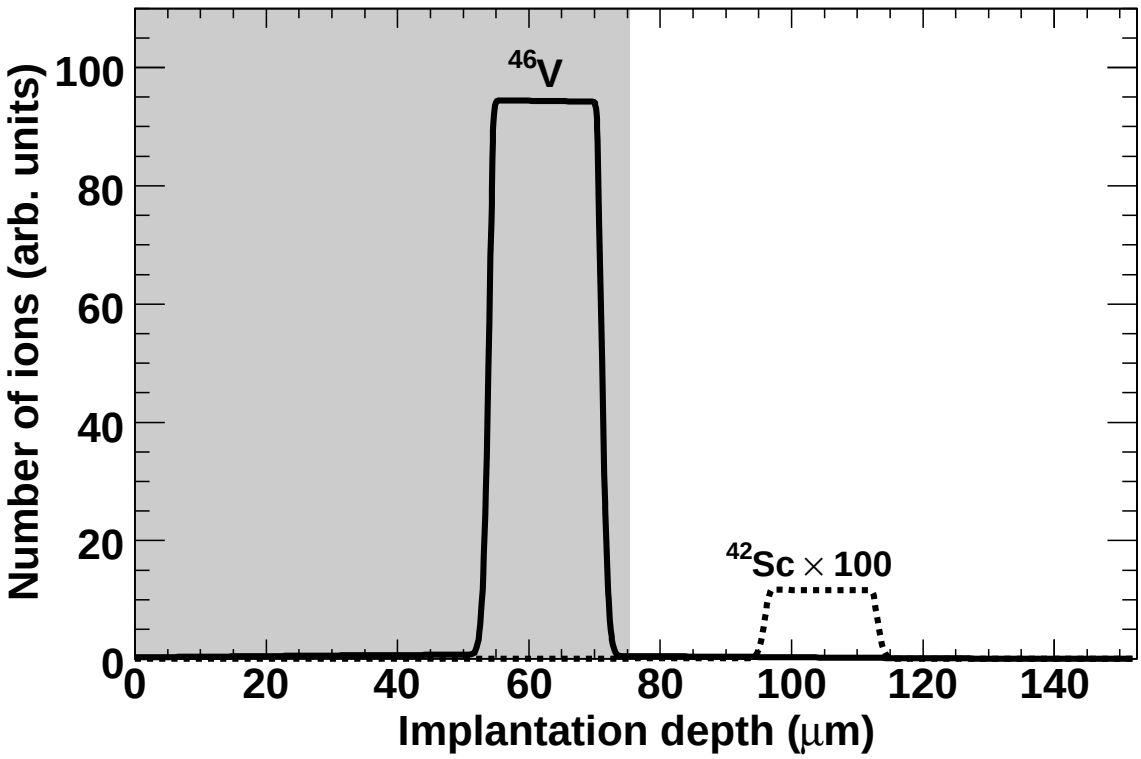

Fig. 14. The implantation profiles of ^{46}V (solid line) and ^{42}Sc (dashed line) in and beyond the Mylar tape, under the conditions applying to our half-life measurements. The beams enter from the left. The shaded region corresponds to the actual thickness of our collection tape: all ions within the shaded region are collected in our sample; all others are not.

fits was very insensitive to the half-life used for ^{46}V, and that, in all cases, the ratio was less than 0.01%.

In arriving at the final half-life for ^{46}V and its uncertainty, we have adopted a very conservative range for the ^{42}Sc/^{46}V ratio, taking the value to be 0.006(6)%.

B. Time-decay analysis

We fitted the data from each of the 16 runs separately, incorporating three components: ^{46}V, ^{42}Sc and a constant background. The half-life of ^{42}Sc was fixed at its known value of 680.72 ms [10] and, as explained in the last section, the initial activity of ^{42}Sc relative to ^{46}V was set at 0.006%. Since each run was obtained with a different combination of detection settings, we could use the individually fitted half-lives of ^{46}V to test for any systematic dependence on those settings. As displayed in Fig. 15, the half-life results showed no systematic dependence on detector bias voltage, discriminator threshold setting, or the dominant dead time we imposed in the electronics, the average half-life yielding a remarkably low value for the normalized χ^2 of 0.2. With this degree of consistency in the data, we can be confident that any systematic dependence on detection parameters must be negligible with respect to our quoted statistical uncertainty.

Our final systematic check was to test for unanticipated short-lived impurities in the decay spectrum or for any other evidence showing count-rate dependence of the half-life. In each run we removed data from the first 0.2 s of the counting period and fitted the remaining data; then we removed an additional 0.2 s of data and refitted again. This procedure was continued until 1.4 s of data – 3.3 half-lives of ^{46}V – had been removed. The average half-life from all 16 runs was then obtained for each set of truncated data. The result is given in Fig. 16 where it can be seen that the half-lives

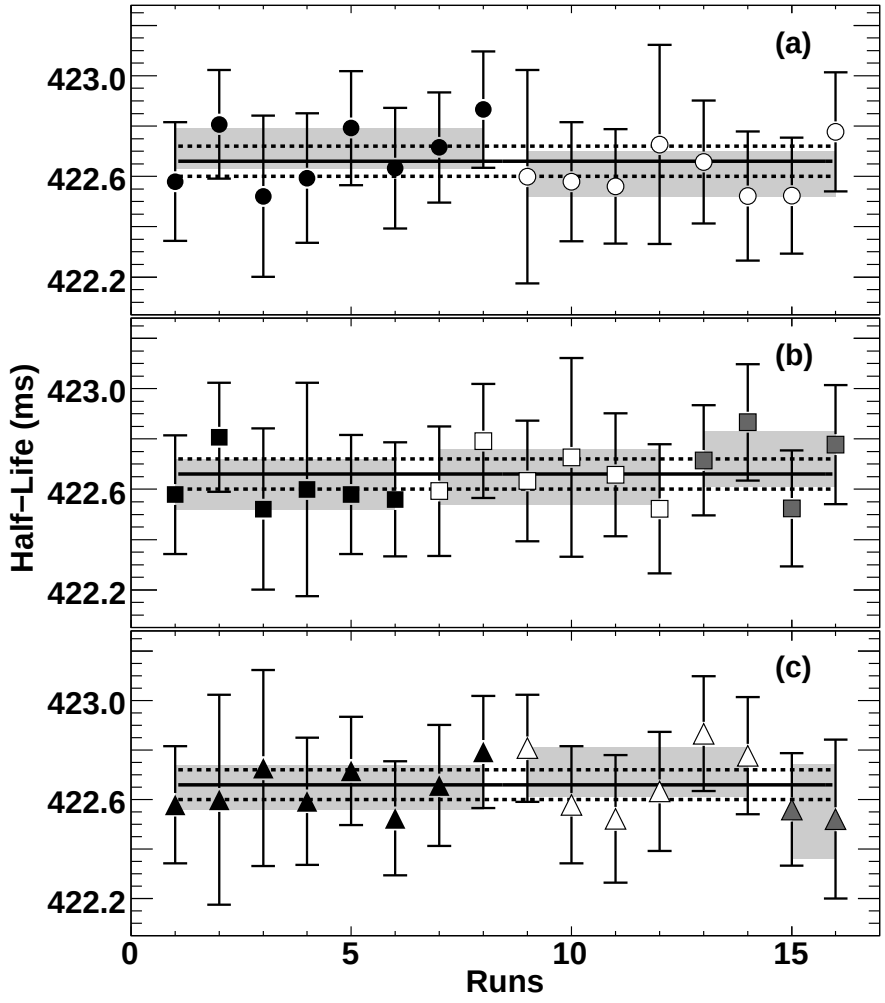

Fig. 15. Test for possible systematic bias in the ^{46}V half-life measurement due to three different detection parameters: (a) two detector biases, 2650 V/2750 V, represented by black/open circles; (b) three discriminator settings, 150 mV/200 mV/250 mV, represented by black/open/grey squares; (c) three imposed dead times, 4μs/6μs/8μs, represented by black/open/grey triangles. Note that the runs have been grouped differently in each part of the figure. In all cases, the grey bands represent the $\pm\sigma$ limits of the average for a given condition. The average value for the half-life is 422.66(6) ms (statistical uncertainty only) with $\chi^2/ndf = 3.3/15$. The average value for all the runs appears as the solid line, with dashed lines as uncertainty limits.

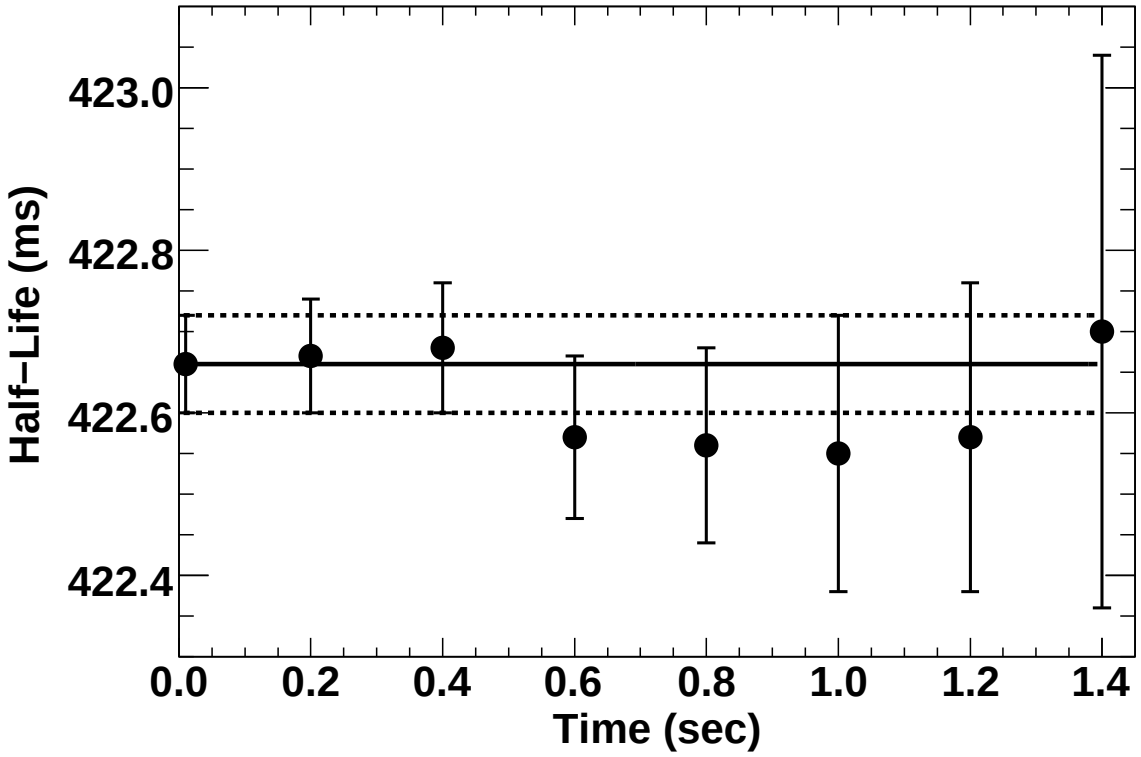

Fig. 16. Test for possible systematic bias in the ^{46}V half-life measurement caused by short-lived impurities or by rate-dependent counting losses that we have not accounted for. Each point is the result of a separate fit to the data; the abscissa for each point represents the time period at the beginning of the counting cycle for which the data were omitted from that particular fit. The solid and dashed lines correspond to the average half-life value and uncertainties given in Fig. 15.

so obtained were consistent with one another within statistical uncertainties.

With these possible systematic effects eliminated as significant factors, our final result for the half-life of ^{46}V is 422.66(6) ms. As shown in Table V, the quoted uncertainty is dominated by counting statistics since the only other identifiable contribution – from a possible ^{42}Sc impurity – is substantially smaller even when very generous limits have been applied (see Sec. V.A).

Table V. Uncertainty budget for the ^{46}V half-life measurement.

Source	Uncertainty (ms)
statistics	0.06
sample impurity (^{42}Sc)	0.02
Total	0.06
^{46}V half-life result (ms)	422.66(6)

C. Comparison with previous results

The quoted precision of our result is 0.014%. There have also been three previous measurements claiming sub 0.1% precision; they yielded half-life values of 422.47(39) ms [49], 422.28(23) ms [50], and 422.57(13) ms [28], all less precise than ours. The first two of these measurements depended on plastic scintillators to detect β particles from the decay, while the third used a very similar technique to ours, with a proportional gas counter used for β detection. Only the latter experiment had assured purity of the decaying sample, having employed an on-line isotope separator to produce it. These three previous results are compared with our new value in Fig. 17. All four values are statistically consistent with one another, with only the result from Ref. [50] lying slightly outside of one standard deviation from the overall average, which is 422.62(05) ms. The normalized χ^2 for the average is a satisfactory 1.0.

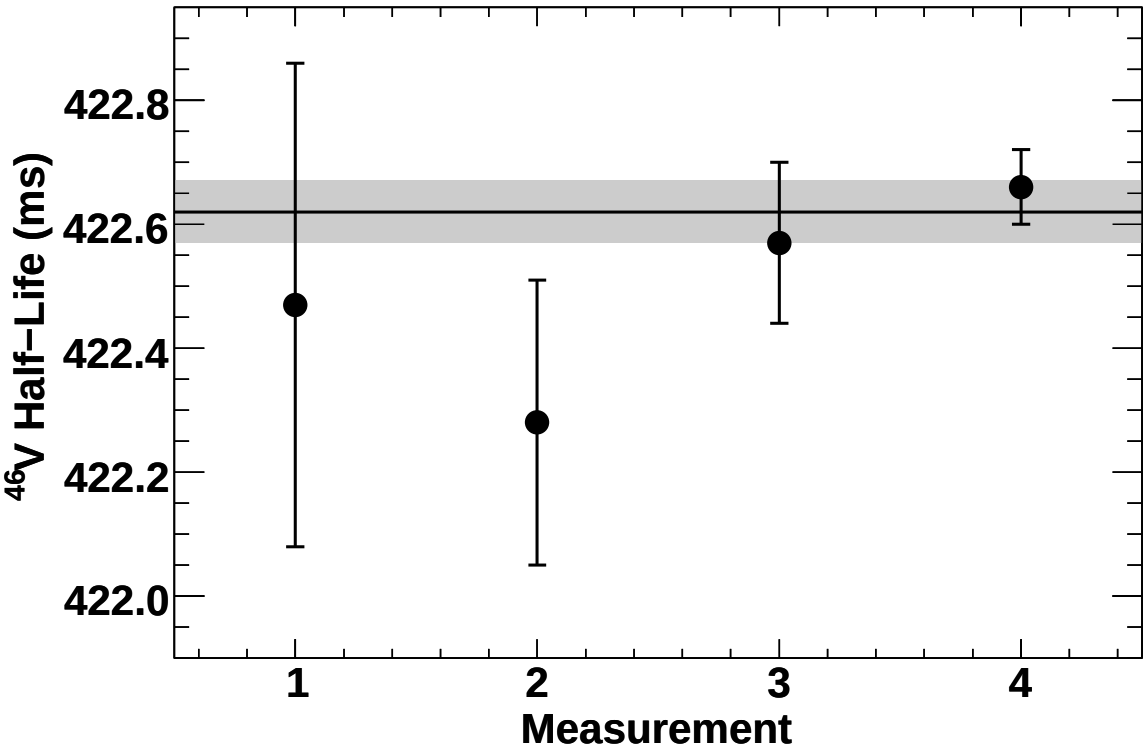

Fig. 17. The present measurement is compared with all the published measurements of ^{46}V half-lives with quoted uncertainties that are within a factor of 10 of our precision. The results are presented in chronological order from left to right. The $\pm\sigma$ limits on the overall average value of 422.62(05) ms appear as the grey band.

CHAPTER VI

BRANCHING RATIO OF ^{38}Ca

The branching ratio for the superallowed transition from a $T_Z = -1$ nucleus must, in principle, be measured with a precision of 0.1%. However, ^{38}Ca is one of a few superallowed decays, for which the total branching ratios of all the non-superallowed branches to excited states in the daughter nucleus sum to a relatively small value ($\sim$20%); thus when this total is subtracted from 100% to yield the value for the superallowed branch, the fractional uncertainty on the latter is reduced. As shown in Fig. 6, the decay of ^{38}Ca populates the analog state (J^π, T) = (0^+, 1) in ^{38}K *via* the superallowed β branch and also populates three (1^+, 0) states fed by Gamow-Teller branches. To precisely determine the branching ratio for the superallowed transition in this particular case, our first step was to obtain the absolute intensities of the three γ rays (*i.e.*, $\gamma_1 = 328$ keV, $\gamma_2 = 1568$ keV and $\gamma_3 = 3211$ keV) that follow the decay of ^{38}Ca *via* three Gamow-Teller transitions (*i.e.*, β_1, β_2 and β_3 respectively). Then the β-branching ratio, R_i, for population of a particular excited state, i, that decays by emitting γ ray, γ_i, can be determined from the following relationship:

$$R_i = \frac{N_{\beta\gamma_i}}{N_\beta \epsilon_{\gamma_i}} k_i \qquad (i = 1, 2, 3), \tag{6.1}$$

where $N_{\beta\gamma_i}$ is the number of γ_i rays observed in coincidence with betas; N_β is the number of (singles) betas observed; ϵ_{γ_i} is the efficiency of the HPGe detector for the γ_i rays; and k_i is a factor ($\sim$1) that accounts for small experimental corrections. With the R_i determined, the sum of all three branching ratios for the Gamow-Teller transitions can be subtracted from 100% to extract the branching ratio for the superallowed transition from ^{38}Ca.

A. Data selection

From a seven-day run, approximately 7.0 million β-γ coincidence events were collected together with over 300 million β singles in 50 separate runs, including 3 runs for room background measurements. As we had changed the gain for the β spectra during the measurement, the data were carefully screened run by run to verify the proper gains and thresholds from the β-γ coincidence spectra and to check for anomalies from the β-γ coincidence time spectra before beginning the analysis. Of the 50 runs, we excluded 25 of them in which the gain was set too high for the β spectra.

Further examination of the data revealed an unexpected problem. Among the total number of events that triggered β-γ coincidences, approximately 20% of the events were not recorded as complete events in our data acquisition system because either the β or γ energy (or both) was below the threshold of the corresponding ADC. This not only limited significantly the precision of our measurement but also required special care in analyzing the data.

Fortunately, we could use the analog scaler record of β-γ coincidences as well as β singles, which were recorded in parallel with data collection in the computer, to correct for the loss of coincident events. Since we had not anticipated that the analog scaler readings would be a vital component of our detailed analysis, occasionally the analog scaler was not gated together with the data acquisition computer when the beam was tuned for a short period. For this reason, the data collected under that condition had to be removed. We compared the number of (singles) betas N_β^{ANALOG}, which was obtained from the analog scaler, with the number of (singles) betas N_β^{DAQ}, which was recorded from the scaler of our data acquisition system and sent directly to the computer. The ratio $N_\beta^{ANALOG}/N_\beta^{DAQ}$ was required to be equal to one within 1%, a condition that led to the rejection of 7 runs. The final spectrum of β-delayed γ

rays observed in coincidence with positrons following the decay of ^{38}Ca was obtained by summing the individual coincidence spectra from all accepted runs.

Our method is now incorporated into the following expression, which accounts for the dead time effects in the data acquisition system and for the effective threshold in analog-to-digital conversion:

$$R_i = I^{ANALOG} \times I_i^{DAQ} \times \frac{k_i}{\epsilon_{\gamma_i}} \qquad (i = 1, 2, 3), \tag{6.2}$$

with

$$\begin{aligned} I^{ANALOG} &= \left(\frac{N_{\beta\gamma}}{N_\beta} \right)^{ANALOG} \\ I_i^{DAQ} &= \left(\frac{N_{\beta\gamma_i}}{N_{\beta_{TDC}}} \right)^{DAQ} \qquad (i = 1, 2, 3). \end{aligned} \tag{6.3}$$

where $N_{\beta\gamma}^{ANALOG}$ is the number of all γ rays in coincidence with betas as recorded in the analog scaler; N_β^{ANALOG} is the number of β singles as recorded in the analog scaler; and $N_{\beta_{TDC}}^{DAQ}$ is the number of betas recorded in the data acquisition computer within the coincidence time, but with no requirement of a γ-ray partner in the recorded spectrum. Note the other notation is defined following Eq. 6.1.

B. Measured intensity

Fig. 18 presents the γ-ray spectrum observed in coincidence with betas, showing the three γ peaks, 328 keV, 1568 keV and 3211 keV, that are attributable to ^{38}Ca. To obtain these areas, all three γ peaks were analyzed with GF3, the least-squares peak-fitting program in the RADWARE [51] package. A Gaussian peak with a smoothed step function and a linear background in the peak region were sufficient to properly describe the data in the spectrum.

In the fit, it was especially important that we determine a reliable background in

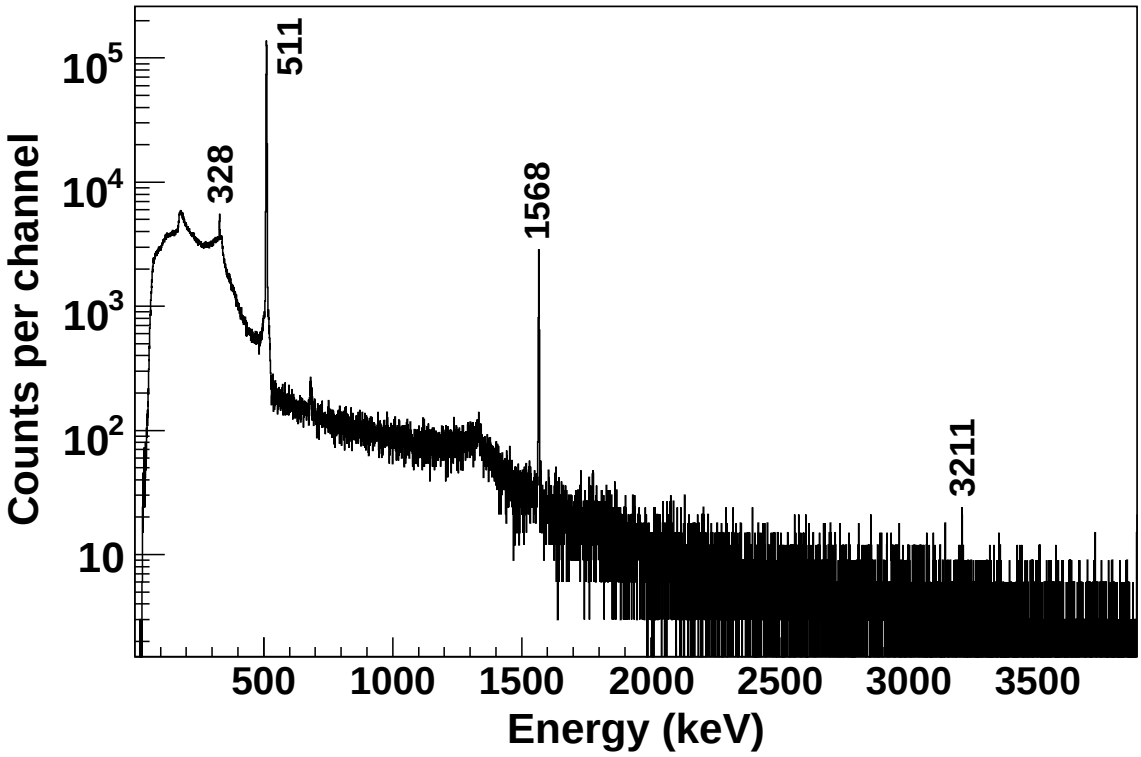

Fig. 18. Spectrum of β-delayed γ rays observed in coincidence with positrons following the decay of ^{38}Ca. The peaks attributable to ^{38}Ca are marked with their energy in keV. The small unmarked peak at 682 keV is caused by summing of one 511-keV γ ray with the back-scattered γ ray (171 keV) from the second 511-keV γ ray.

the 300-keV region because the 328-keV γ-ray full-energy peak is located close to the Compton edge of the scattering distribution from the 511-keV positron-annihilation γ rays. This was accomplished by our measuring the β-delayed γ-ray spectrum from a 40-μC ^{22}Na source, which emits only single 1275-keV γ ray to the ground state of ^{22}Na apart from the 511-keV positron-annihilation γ rays. Fig. 19 displays the measured γ-ray spectrum of ^{22}Na. For the energy range between 200 keV and 400 keV, we compared the spectrum of ^{22}Na with that of ^{38}Ca. The result verified that no unexpected structure lay beneath the 328-keV γ peak in the ^{38}Ca γ-ray spectrum.

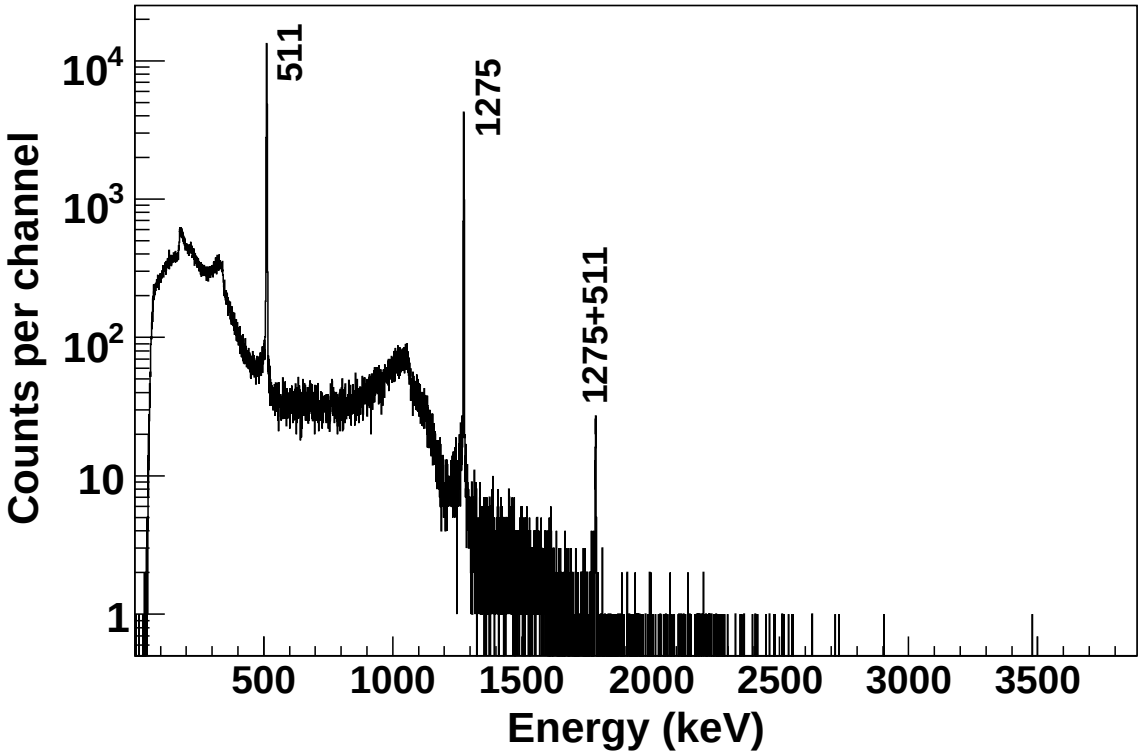

Fig. 19. Measured γ-ray spectrum of ^{22}Na with a 40-μC ^{22}Na source. The peaks attributable to ^{22}Na are marked with their energy in keV; The sum peak is identified by its component.

Table VI. Measured intensity ratios, I_i, and known γ-ray efficiencies, ϵ_{γ_i}, for the three Gamow-Teller transitions from ^{38}Ca.

E_{γ_i}	I_i	ϵ_{γ_i}
328	0.0290(3)	0.0054
1568	0.1828(14)	0.0018
3211	0.0036(3)	0.0009

Combined with the our HPGe detector efficiencies calibrated to the precision of 0.2% in the energy range of interest, our experimental values of $I_i = I^{ANALOG} \times I_i^{DAQ}$ from Eq. 6.3 for 328-keV, 1568-keV and 3211-keV rays are shown in Table VI.

C. Experimental corrections

The correction factor k_i must be evaluated to achieve high precision in determining the branching ratio. For our measurement, k_i is really a product of four separate corrections: random coincidences (k_i^{random}); real-coincidence summing ($k_i^{summing}$); energy dependence of the β-detector response function ($k_i^{\beta_{eff}}$); and γ-ray pile-up ($k_i^{\gamma-pileup}$). With $k_i = k_i^{random} \times k_i^{summing} \times k_i^{\beta_{eff}} \times k_i^{\gamma-pileup}$, we determined the correction factor in Eq. 6.2 to be $k_1 = 1.0304(203)$, $k_2 = 1.0351(160)$ and $k_3 = 0.8365(1094)$, respectively. Each component of these corrections will be discussed individually.

1. Random coincidences (k_i^{random})

There is a finite probability that the two separate events from independent decays occur closely spaced in time and are counted as a coincidence. We can correct for these random coincidences because the time intervals separating adjacent such events are randomly distributed. For each coincident event, we recorded the time between

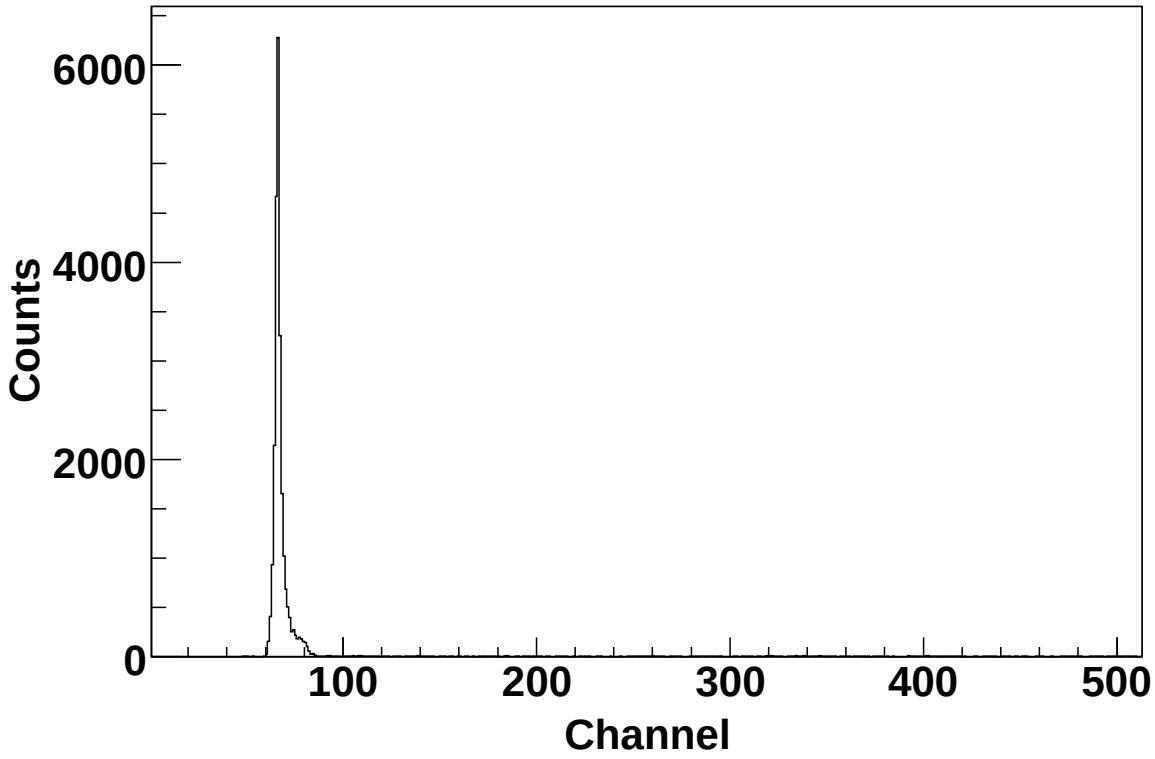

Fig. 20. Time spectrum corresponding to the 1568-keV γ ray based on the time between each coincident β particle and γ ray, being recorded event by event.

the beta and γ-ray signals. This time spectrum for the 1568 keV γ ray is shown in Fig 20, where the prompt coincidence peak stands prominently above the flat random distribution, allowing us clearly to determine the relative contributions of real and random coincidences. The correction factor for the random contribution to the β-coincident 1568-keV γ-ray peak is $k_2^{random} = 0.987(12)$. For the other two γ rays at 328 keV and 3211 keV, we repeated the same procedure and the correction factors were determined to be $k_1^{random} = 0.986(17)$ and $k_3^{random} = 0.79(10)$, respectively.

2. Real-coincidence summing ($k_i^{summing}$)

Coincidence summing occurs when two γ rays from the same decay reach the HPGe detector simultaneously and are recorded as a single γ ray with the combined energy of

both. In our case, all three γ rays, 328-keV, 1568-keV and 3211-keV, are accompanied by a positron from the ^{38}Ca β^+-decay branch that populated the states. Thus all three γ rays have a significant probability for summing with 511-keV annihilation radiation, thus removing events from the corresponding photopeak. The 2079-keV (1568 + 511) γ ray was the only sum peak clearly visible in our β-coincident γ-ray spectrum. To account for the unavoidable loss from the 1568-keV photopeak, our first step was to extract the area of the observed 2079-keV sum peak. Then we multiplied the sum-peak area by the known "total-to-peak" ratio for our detector at 511 keV [33] to include the correction for losses from the 1568-keV γ ray, caused by the 511-keV photopeak's Compton scattered radiation. The total loss due to real-coincidence summing was determined to be 2.33%, *i.e.*, $k_i^{summing} = 1.0233(2)$. This value was used for all three photopeaks.

3. Beta-detector response function ($k_i^{\beta_{eff}}$)

It is necessary to take account of the difference in the β-detection efficiency from one β transition to another, which would affect the measured intensity of coincident γ rays following that β transition. The weak energy dependence of our β-detection efficiency, caused by our low-energy electronic threshold, was examined with the Monte Carlo code EGSnrc [42]. Our geometry of tape and β-detector was used to simulate the β^+ energy spectra for three individual branches (β_1, β_2 and β_3) as well as for the total with all branches included. At a fixed threshold ($\sim$ 80 keV), a different fraction of the betas are lost for transitions with different β end-point energies. Although the change in this loss is small from one transition to another, it is not negligible. The correction factor for each branch is the ratio of the total β-detection efficiency relative

Table VII. The deduced branching ratios for the β-decay of ^{38}Ca.

E_{γ_i}	$E_x(^{38}K)$	R_i
328	459	0.0299(7)
1568	1698	0.1893(34)
3211	3341	0.0028(4)

to the β-detection efficiency for that branch:

$$k_i^{\beta_{eff}} = \frac{\epsilon_{\beta_{total}}}{\epsilon_{\beta_i}} \qquad (i = 1, 2, 3), \tag{6.4}$$

where ϵ_{β_1}, ϵ_{β_2} and ϵ_{β_3} are the detector efficiencies for the β transitions to the first, second and third excited states in ^{38}K, respectively. We determined the correction factors to be $k_1^{\beta_{eff}} = 0.9962(10)$, $k_2^{\beta_{eff}} = 1.0002(10)$ and $k_3^{\beta_{eff}} = 1.0130(48)$.

4. Pile up ($k_i^{\gamma-pileup}$)

Because of the relatively slow electronics used for γ ray counting, pile-up of two uncorrelated γ-rays causes some loss of events. We estimated this effect as being equal to τN, where τ is the total γ-ray pulse length ($\sim$12 μs) and N is the γ-ray singles rate ($\sim 2\times10^3$ counts/s). The correction factor thus becomes $k_i^{\gamma-pileup} = 1.025(10)$.

D. Results

When combined in Eq. 6.2 with the experimental correction factors already discussed, our results of the β-branching ratio for the three Gamow-Teller branches are given in Table VII. We further adopted the eight additional measured γ-ray intensities ($\sim$2% in total) from Ref. [37] and normalized them to the most intense branch (β_2) measured

from our work. The sum of all branching ratios for the transitions populating excited states in ^{38}K was determined to be 22.62(41)%. The subtraction of this value from 100% yields the result for the branching ratio of the superallowed branch:

$$R_{SA} = 77.38(41)\%. \tag{6.5}$$

CHAPTER VII

CONCLUSIONS AND FUTURE DIRECTIONS

A. Experimental tests of the nuclear-structure-dependent corrections for ^{38}Ca

We report here the half-life of the superallowed β^+ emitter ^{38}Ca to be 443.88(36) ms, the first time it has been measured with a precision of better than 0.1%. Since ^{38}Ca and its daughter ^{38}K^m are both positron emitters and have comparable half-lives, we analyzed their decay using a technique we developed previously [26, 39], in which the parent and daughter decays can be linked by means of a precise measurement of the deposition rate of each 99.6%-pure ^{38}Ca sample. The major contributions to our overall uncertainty came from the uncertainties in the known half-life of ^{38}K^m and in our experimental determination of the relative intensity of the small ^{35}Ar contaminant in our collected ^{38}Ca sources. We determined the branching ratio for the superallowed transition of ^{38}Ca to be 77.38(41)%. This result was derived by subtracting from 100% the total, 22.62(41)%, of all non-superallowed branches leading to γ rays whose absolute intensities were measured experimentally. The benefit of this approach is that we require only 0.3% precision in our measurement of non-superallowed branches to achieve the desired precision of 0.1% on the superallowed branching ratio.

Before our half-life and branching-ratio measurement of ^{38}Ca, which is presented here, only its Q_{EC} value was known to the desired precision: it had been measured with Penning-traps to $\pm$0.006% [3, 4, 5], which corresponds to an f-value precision of $\pm$0.03% [10]. The most precise half-life result was only known to $\pm$0.4% [48] and the superallowed branching ratio had not yet been measured at all. Now, we have measured the ^{38}Ca half-life to $\pm$0.08% and presented the superallowed branching ratio of ^{38}Ca to $\pm$0.5%. Together with other properties, the Q_{EC} value and theoretical

corrections for radiative and isospin-symmetry breaking effects taken from Ref [10], our half-life and branching-ratio results yield an $\mathcal{F}t$ value of 3072(17) s for the superallowed transition from ^{38}Ca. This result agrees with the average $\overline{\mathcal{F}t}$ value of 3072.08(79) s established from 13 well-known superallowed transitions [10].

Fig. 21 shows the current contributions of individual experimental and theoretical uncertainties to the final $\mathcal{F}t$-value uncertainty of ^{38}Ca. The experimental quantities of the half-life and branching ratio in this figure depend only on our results for ^{38}Ca. The branching ratio remains to be measured with $\sim$0.1% precision before this transition can take its place with the best-known superallowed transitions. For this goal, we are currently implementing various improvements to our data-acquisition electronics. One of our major focuses is to independently measure deadtimes by recording the number of β-γ coincidence triggers in the data stream on cycle-by-cycle basis. Another effort involves the optimization of the discrimination level for a truly coincident β-γ pair of events which arrive at their corresponding ADC concurrently. The valid events must be discriminated from noise background without any losses. We are also planning to employ the pulser method for measuring pile-up losses in the coincident γ rays. Once these improvements have been made, we will be one step closer to improving the precision by a factor of 5 for the branching-ratio measurement of ^{38}Ca.

With its relatively large calculated structure-dependent corrections, it will then contribute significantly to a comparative evaluation of the various sets of calculated correction terms [21], the ultimate goal being to reduce the uncertainties on these correction terms and consequently improve the precision of the CKM-matrix unitarity test.

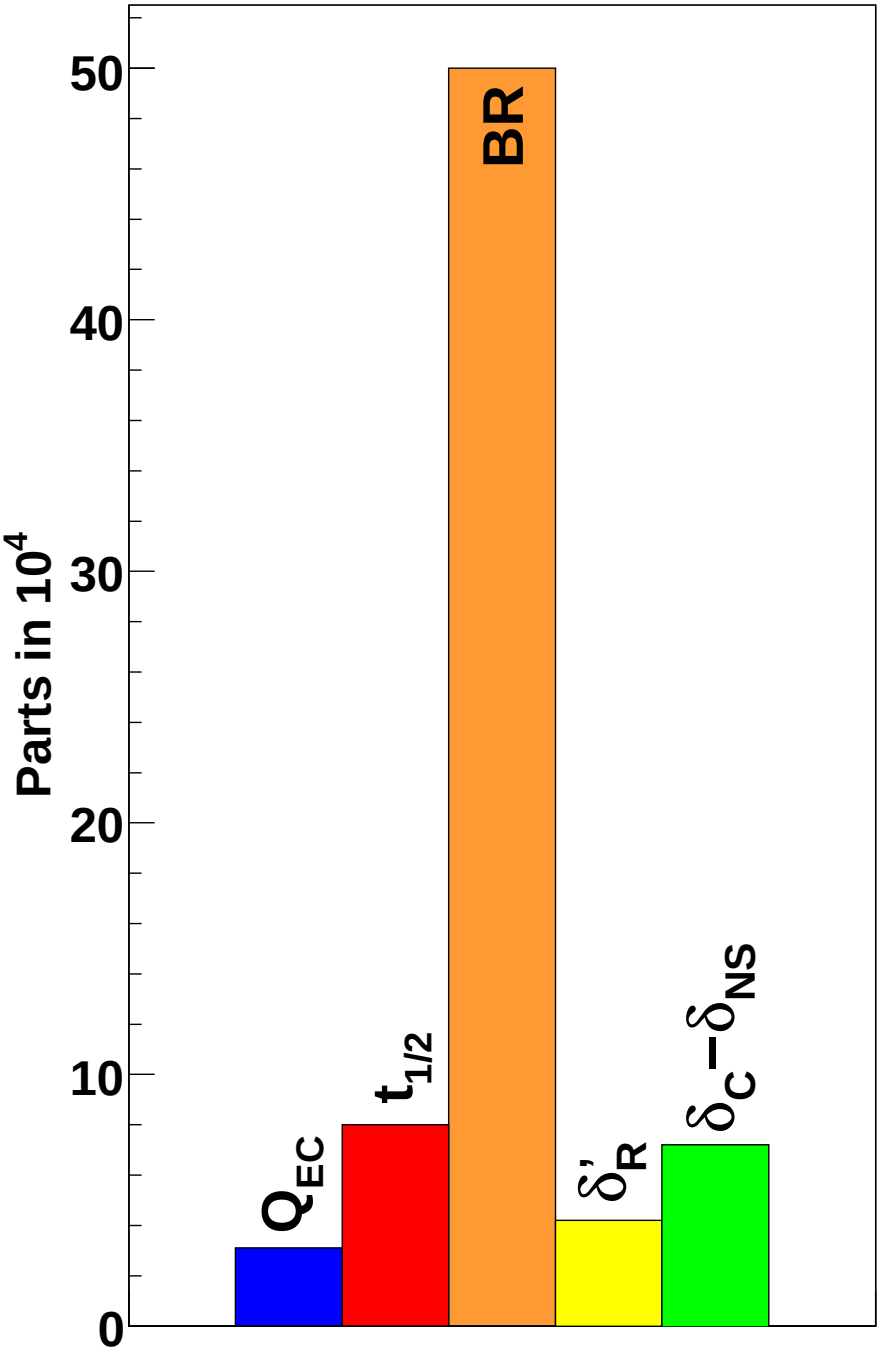

Fig. 21. Summary histogram of the fractional uncertainties attributable to each experimental and theoretical input factor that contributes to the final $\mathcal{F}t$ value for the superallowed transition of ^{38}Ca. Only our new results were considered for the measured half-life and branching-ratio contributions.

B. Present status of $\mathcal{F}t$ value for ^{46}V

We have measured a new value for half-life of the superallowed β^+ emitter ^{46}V. Our result, 422.66(6) ms, is a factor of two more precise than the best previous result, with which it is completely consistent. If our half-life value is combined with previous measurements of the same quantity, it yields a new world average of 422.62(05) ms. The other properties of this decay – its Q_{EC} value, branching ratio and the calculated corrections for radiative and isospin-symmetry breaking effects – have been tabulated recently in Ref. [10]. Combining the new world-average half-life with these tabulated values we obtain a corrected $\mathcal{F}t$ value for the ^{46}V superallowed transition of 3074.2(26) s, where the uncertainty is dominated by the uncertainties applied to the theoretical correction terms (see Fig. 22). This result is entirely consistent with the average $\overline{\mathcal{F}t}$ value of 3072.08(79) s established in the most recent survey [10] of world data from 13 well-known superallowed transitions as shown in Fig 23.

Evidently, the important experimental components of the ^{46}V superallowed transition – its half-life and Q_{EC} value – have now been satisfactorily confirmed and improved. The $\mathcal{F}t$ value for this transition is certainly not anomalous at the 0.08% level of precision currently quoted on that quantity.

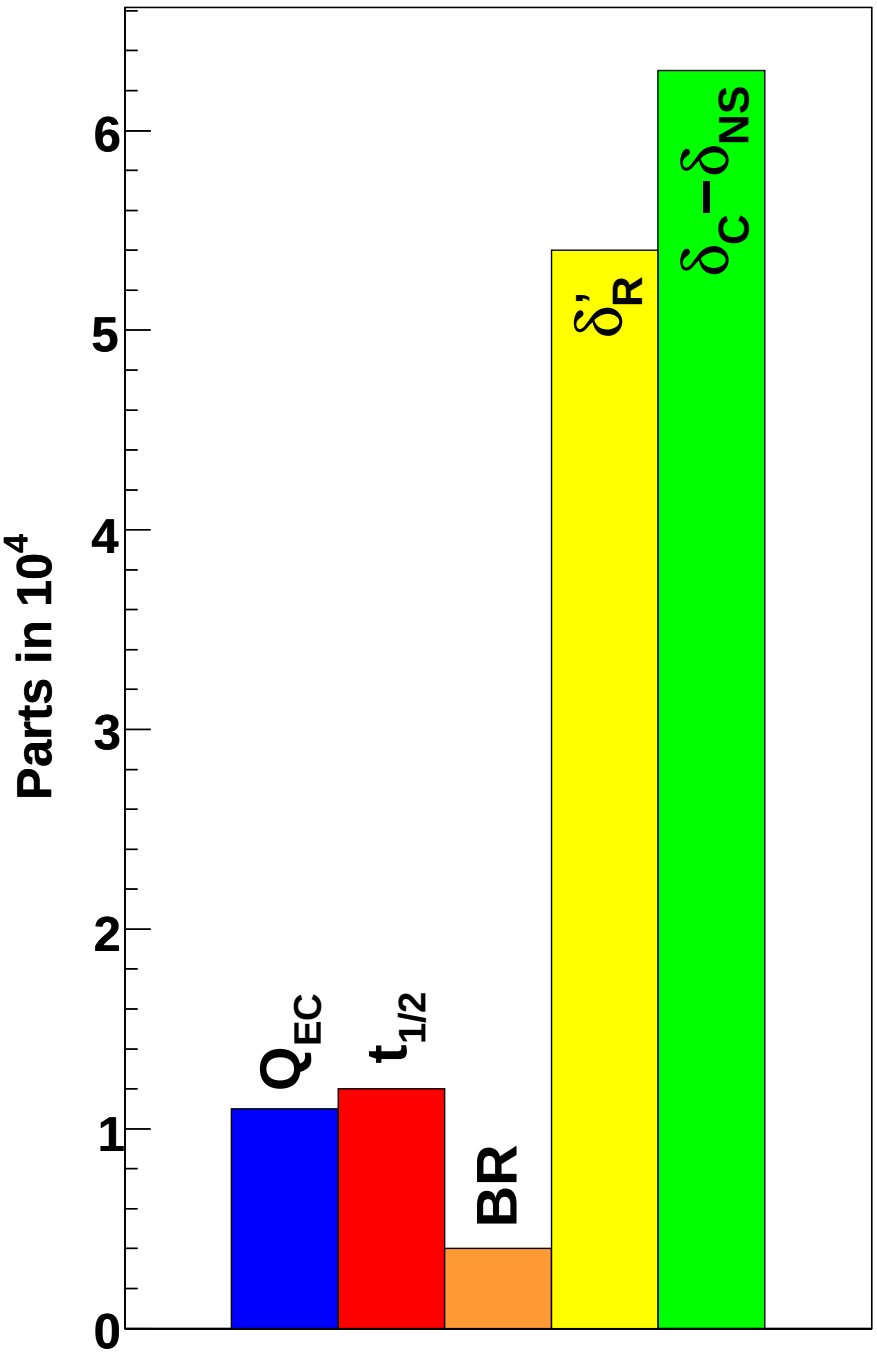

Fig. 22. Summary histogram of the fractional uncertainties attributable to each experimental and theoretical input factor that contributes to the final $\mathcal{F}t$ value for the superallowed transition of ^{46}V. This figure has been updated from Ref [10] with our half-life measurement included.

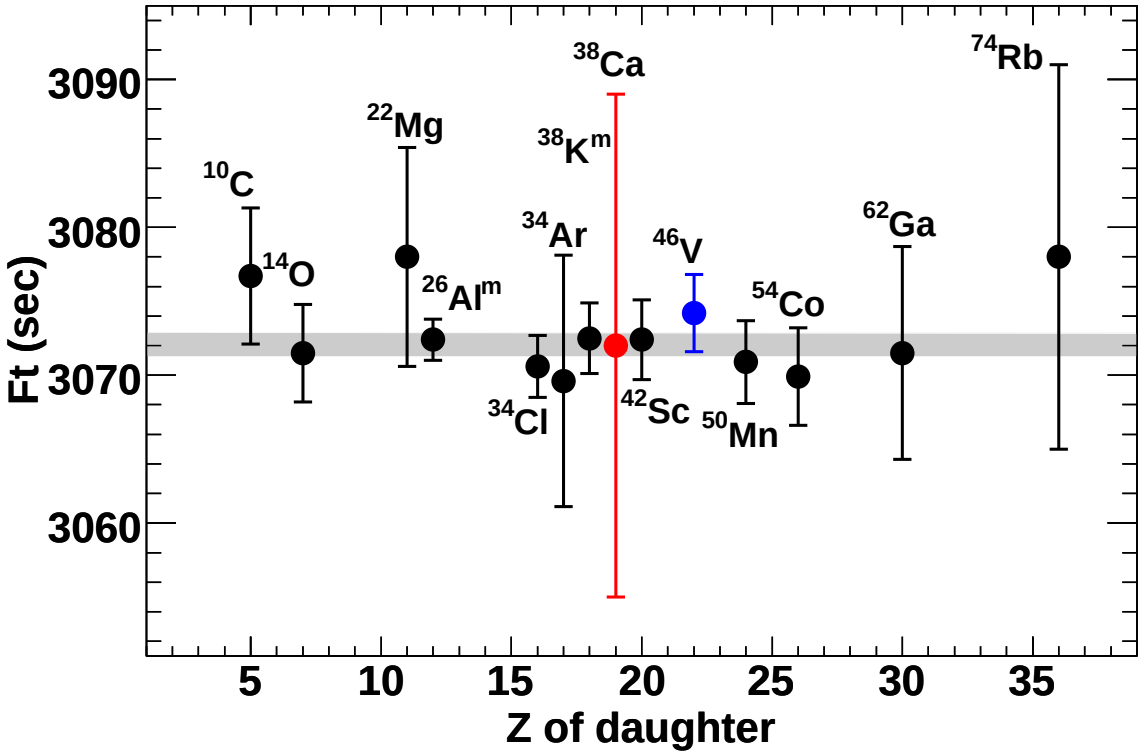

Fig. 23. $\mathcal{F}t$ values ploted as a function of the proton number on the daughter nucleus Z. The grey band represents one standard deviation around the average $\overline{\mathcal{F}t}$ value of 3072.08(79) s obtained from the 13 best-known superallowed transitions. With the half-life and branching ratio of ^{38}Ca measured from this work, the corresponding $\mathcal{F}t$ value for the ^{38}Ca transition was determined. The $\mathcal{F}t$ value for the ^{46}V transition was updated with our new precise half-life measurement.

REFERENCES

[1] I.S. Towner and J.C. Hardy, Rep. Prog. Phys. **73**, 046301 (2010).

[2] I.S. Towner and J.C. Hardy, Phys. Rev. C **77**, 025501 (2008).

[3] G. Bollen, D. Davies, M. Facina, J. Huikari, E. Kwan, P.A. Lofy, D.J. Morrissey, A. Prinke, R. Ringle, J. Savory, P. Schury, S. Schwarz, C. Sumithrarachchi, T. Sun and L. Weissman, Phys. Rev. Lett. **96**, 152501 (2006).

[4] R. Ringle, T. Sun, G. Bollen, D. Davies, M. Facina, J. Huikari, E. Kwan, D.J. Morrissey, A. Prinke, J. Savory, P. Schury, S. Schwarz and C.S. Sumithrarachchi, Phys. Rev. C **75**, 055503 (2007).

[5] S. George, S. Baruah, B. Blank, K. Blaum, M. Breitenfeldt, U. Hager, F. Herfurth, A. Herlert, A. Kellerbauer, H.-J. Kluge, M. Kretzschmar, D. Lunney, R. Savreux, S. Schwarz, L. Schweikhard and C. Yazidjian, Phys. Rev. Lett. **98**, 162501 (2007).

[6] G. Savard, F. Buchinger, J.A. Clark, J.E. Crawford, S. Gulick, J.C. Hardy, A.A. Hecht, J.K.P. Lee, A.F. Levand, N.D. Scielzo, H. Sharma, K.S. Sharma, I. Tanihata, A.C.C. Villari, and Y. Wang, Phys. Rev. Lett. **95**, 102501 (2005).

[7] H. Vonach, P. Glassel, E. Huenges, P. Maier-Komor, H. Rosler, H.J. Scheerer, H. Paul and, D. Semrad, Nucl. Phys. **A278**, 189 (1977).

[8] T. Eronen, V. Elomaa, U. Hagar, J. Hakala, A. Jokinen, A. Kankainen, I. Moore, H. Penttila, S. Rahaman, J. Rissanen, A. Saastamoinen, T. Sonoda, J. Aysto, J.C. Hardy, and V.S. Kolhinen, Phys. Rev. Lett. **97**, 232501 (2006).

[9] T. Faestermann, R. Hertenberger, H.-F. Wirth, R. Krücken, M. Mahgoub, and P. Maier-Komor, Eur. Phys. J. A **42**, 339 (2009).

[10] J.C. Hardy and I.S. Towner, Phys. Rev. C **79**, 055502 (2009).

[11] E.D. Commins and P.H. Bucksbaum, *Weak Interactions of Leptons and Quarks*, (Cambridge University Press, Cambridge, 1983).

[12] E. Fermi, Z. Phys. **88**, 161 (1934).

[13] C.S. Wu, Rev. Mod. Phys. **36**, 618 (1964).

[14] R. Feynman and M. Gell-Mann, Phys. Rev. **109**, 193 (1958).

[15] C.S. Wu and S.A. Moszkowski, *Beta Decay*, (John Wiley & Sons, Inc., New York, 1966).

[16] N. Cabibbo, Phys. Rev. Lett. **10**, 531 (1963).

[17] M. Kobayashi and T. Maskawa, Prog. Theor. Phys. **49**, 652 (1973).

[18] E.P. Wigner, Phys. Rev. **56**, 519 (1939).

[19] I.S. Towner and J.C. Hardy, Phys. Rev. C **66**, 035501 (2002).

[20] W.J. Marciano and A. Sirlin, Phys. Rev. Lett. **96**, 032002 (2006).

[21] I.S. Towner and J.C. Hardy, Phys. Rev. C **82**, 065501 (2011).

[22] C. Amsler, M. Doser, M. Antonelli, D.M. Asner, K.S. Babu, *et al.* (Particle Data Group), Phys. Lett. B **667**, 1 (2008).

[23] A. Serebrov, V. Varlamov, A. Kharitonov, A. Fomin, Yu. Pokotilovski, P. Geltenbort, J. Butterworth, I. Krasnoschekova, M. Lasakov, R. Tal'daev, A. Vassiljev and O. Zherebtsov, Phys. Lett. B **605**, 72 (2005).

[24] S. Arzumanov, L. Bondarenko, S. Chernyavsky, W. Drexel, A. Fomin, P. Geltenbort, V. Morozov, Yu. Panin, J. Pendlebury, K. Schreckenbach, Phys. Lett. B **483**, 15 (2000).

[25] R.E. Tribble, R.H. Burch and C.A. Gagliardi, Nucl. Instr. and Meth. in Phys. Res. A **285**, 441 (1989).

[26] V.E. Iacob, J.C. Hardy, J.F. Brinkley, C.A. Gagliardi, V.E. Mayes, N. Nica, M. Sanchez-Vega, G. Tabacaru, L. Trache and R.E. Tribble, Phys. Rev. C **74**, 055502 (2006).

[27] R. Brun, and F. Rademakers Nucl. Instr. and Meth. in Phys. Res. A **389**, 81 (1997).

[28] V.T. Koslowsky, E. Hagberg, J.C. Hardy, G. Savard, H. Schmeing, K.S. Sharma and X. J. Sun, Nucl. Instr. and Meth. in Phys. Res. A **401**, 289 (1997).

[29] F. James, "MINUIT: Function Minimization and Error Analysis," Reference Manual, Version 94.1 (CERN, Geneva, 1998).

[30] K. Siegbahn, *Beta- and Gamma-Ray Spectroscopy*, (North-Holland Publishing Company, Amsterdam, 1955).

[31] V.E. Iacob, J.C. Hardy, C.A. Gagliardi, J. Goodwin, N. Nica, H.I. Park, G. Tabacaru, L. Trache, R.E. Tribble, Y. Zhai and I.S. Towner, Phys. Rev. C **74**, 015501 (2006).

[32] V.V. Golovko, V.E. Iacob, J.C. Hardy, Nucl. Instr. and Meth. in Phys. Res. A **594**, 266 (2008).

[33] R.G. Helmer, J.C. Hardy, V.E. Iacob, M. Sanchez-Vega, R.G. Neilson, J. Nelson, Nucl. Instr. and Meth. in Phys. Res. A **511**, 360 (2003).

[34] J.C. Hardy, V.E. Iacob, M. Sanchez-Vega, R.T. Effinger,P. Lipnik, V.E. Mayes, D.K. Willis and R.G. Helmer, Int. J. Appl. Radiat. Isot. **56**, 65 (2002).

[35] R.G. Helmer, N. Nica, J.C. Hardy, V.E. Iacob, Int. J. Appl. Radiat. Isot. **60**, 173 (2004).

[36] Sparrow Corporation, http://www.sparrowcorp.com/ (1997).

[37] B.D. Anderson, A.R. Baldwin, P. Baumann, B.A. Brown, F. Didierjean, C.C. Foster, L.A.C. Garcia, A. Huck, R. Madey, D.M. Manley, G. Marguier, M. Ramdhane, H. Ravn, C. Richard-Serre, G. Walter and J.W. Watson, Phys. Rev. C **54**, 602 (1996).

[38] Acuity Laser Measurement, http://www.acuitylaser.com/ (2007).

[39] V.E. Iacob, J.C. Hardy, A. Banu, L. Chen, V.V. Golovko, J. Goodwin, V. Horvat, N. Nica, H.I. Park, L. Trache and R.E. Tribble, Phys. Rev. C **82**, 035502 (2010).

[40] J.A. Cameron and B. Singh, Nuclear Data Sheets **109**, 1 (2008).

[41] K.G. Leach, C.E. Svensson, G.C. Ball, J.R. Leslie, R.A.E. Austin, D. Bandyopadhyay, C. Barton, E. Bassiachvilli, S. Ettenauer, P. Finlay, P.E. Garrett, G.F. Grinyer, G. Hackman, D. Melconian, A.C. Morton, S. Mythili, O. Newman, C.J. Pearson, M.R. Pearson, A.A. Phillips, H. Savajols, M.A. Schumaker and J. Wong, Phys. Rev. Lett. **100**, 192504 (2008).

[42] I. Kawrakow, Med. Phys. **27**, 485 (2000); I. Kawrakow and D.W.O. Rogers, NRCC Report PIRS-701, NRC, Ottawa (2003); http://www.irs.inms.nrc.ca/EGSnrc/ EGSnrc.html.

[43] J.F. Ziegler, http://www.srim.org/ (2008).

[44] R.W. Kavanagh, A. Gallmann, E. Aslanides, F. Jundt and E. Jacobs, Phys. Rev. **175**, 1426 (1968).

[45] A. Gallmann, E. Aslanides, F. Jundt and E. Jacobs, Phys. Rev. **186**, 1160 (1969).

[46] J. Zioni, A.A. Jaffe, E. Friedman, N. Haik, R. Schectman and D. Nir, Nucl. Phys. A **181**, 465 (1972).

[47] H.S. Wilson, R.W. Kavanagh and F.M. Mann, Phys. Rev. C **22**, 1696 (1980).

[48] B. Blank, A. Bey, I. Matea, J. Souin, L. Audirac, M.J.G. Borge, G. Canchel, P. Delahaye, F. Delalee, C.-E. Demonchy, R. Domínguez-Reyes, L.M. Fraile, J. Giovinazzo, Tran Trong Hui, J. Huikari, D. Lunney, F. Munoz, J.-L. Pedroza, C. Plaisir, L. Serani, S. Sturm, O. Tengblad and F. Wenander, Eur. Phys. J. A **44**, 363 (2010).

[49] D.E. Alburger and D.H. Wilkinson, Phys. Rev. C **15**, 2174 (1977).

[50] P.H. Barker, C.J. Scofield, R.J. Petty, J.M. Freeman, S.D. Hoath, W.E. Burcham, and G.T.A. Squier, Nucl. Phys. **A275**, 37 (1977).

[51] D.C. Radford, Nucl. Instr. and Meth. in Phys. Res. A **361**, 297 (1995); http://www.radware.phy.ornl.gov/.

VITA

Hyo-In Park was born in Seoul Korea and received a Bachelor of Science in physics from Colorado State University in 1999. She graduated with the Master of Science in nuclear physics from the University of Tennessee in 2003. The following year, she joined the Cyclotron Institute of Texas A&M University as a graduate research assistant to study nuclear tests of the weak interaction via superallowed beta-decay under the supervision of Distinguished Professor John C. Hardy. At the completion of this dissertation, Hyo-In Park plans to continue her activity in the research field. Her contact mailing address is Cyclotron Institute, Texas A&M University, 3366 TAMU, College Station, Texas 77843.

The typist for this dissertation was Hyo-In Park.